

Population-level Hypothesis Testing with Rocky Planet Emission Data: A Tentative Trend in the Brightness Temperatures of M-Earths

BRANDON PARK COY ¹, JEGUG IH ^{2,3}, EDWIN S. KITE ¹, DANIEL D.B. KOLL ⁴, MORITZ TENTHOFF ⁵,
JACOB L. BEAN ⁶, MEGAN WEINER MANSFIELD ^{7,2}, MICHAEL ZHANG ⁶, QIAO XUE ⁶, ELIZA M.-R. KEMPTON ²,
KAY WOHLFARTH ⁵, RENYU HU ^{8,9}, XINTONG LYU ⁴ AND CHRISTIAN WÖHLER⁵

¹*Department of the Geophysical Sciences, University of Chicago, Chicago, IL, USA*

²*Department of Astronomy, University of Maryland, College Park, MD, USA*

³*Space Telescope Science Institute, Baltimore, MD, USA*

⁴*Department of Atmospheric and Oceanic Sciences, Peking University, Beijing, People's Republic of China*

⁵*Department of Electrical Engineering and Information Technology, Technische Universität Dortmund, Dortmund, Germany*

⁶*Department of Astronomy & Astrophysics, University of Chicago, Chicago, IL, USA*

⁷*School of Earth and Space Exploration, Arizona State University, Tempe, AZ, USA*

⁸*Jet Propulsion Laboratory, Pasadena, CA, USA*

⁹*Division of Geological and Planetary Sciences, California Institute of Technology, Pasadena, CA, USA*

ABSTRACT

Determining which rocky exoplanets have atmospheres, and why, is a key goal for JWST. So far, emission observations of individual rocky exoplanets orbiting M stars (M-Earths) have not provided definitive evidence for atmospheres. Here, we synthesize emission data for M-Earths and find a trend in measured brightness temperature (ratioed to its theoretical maximum value) as a function of instellation. However, the statistical evidence of this trend is dependent on the choice of stellar model and we consider its identification tentative. We show that this trend can be explained by either the onset of thin/tenuous atmospheres on colder worlds, or a population of bare rocks with stronger space weathering and/or coarser regolith on closer-in worlds. Such grain coarsening may be caused by sintering near the melting point of rock or frequent volcanic resurfacing. We also find that fresh, fine-grained surfaces can serve as a false positive to the detection of moderate atmospheric heat redistribution. However, we argue that such surfaces are unlikely given the ubiquity of space weathering in the Solar System and the low albedo of Solar System airless bodies. Furthermore, we highlight considerations when testing rocky planet hypotheses at the population level, including the choice of instrument, stellar modeling, and how brightness temperatures are derived. Emission data from a larger sample of M-Earths will be able to confirm or reject this tentative trend and diagnose its cause.

Keywords: Exoplanets (498), James Webb Space Telescope (2291), Exoplanet atmospheres (487), Extrasolar rocky planets (511)

1. INTRODUCTION

A key goal for the James Webb Space Telescope (JWST) is to determine the prevalence and origins of terrestrial (i.e., “rocky”, smaller than $1.5 R_{\oplus}$) exoplanet atmospheres. Toward this goal, studying terrestrial exoplanets orbiting M dwarfs (“M-Earths”) is crucial, as these stars are the most abundant in our neighborhood

and their favorable signal sizes are currently the most amenable to investigating potentially habitable worlds (Seager 2013; Barstow & Irwin 2016; Lustig-Yaeger et al. 2019).

Observing the thermal emission of tidally-locked rocky exoplanets in secondary eclipse allows for efficient detection of atmospheres on such worlds (Koll et al. 2019; Mansfield et al. 2019). Secondary eclipse observations allow for measuring a planet’s dayside temperature, which can constrain the amount of incident heat redistributed to the nightside by the atmosphere. As a thick

atmosphere should cool the dayside by redistributing heat over the entire planet, observing a colder dayside than expected for a ‘bare rock’ planet can indicate the presence of an atmosphere. This effect is evident in the non-tidally locked Solar System terrestrial planets (e.g., see Figure 4 of [Xue et al. 2024](#)). Additionally, high albedo cloud decks, like those on Venus, would further cool the planet’s dayside.

Beyond their detection, characterizing the atmosphere is also potentially viable. As many gas species expected in rocky planet atmospheres (e.g., CO_2 , H_2O , SO_2) are infrared absorbers, they both control the vertical thermal structure of the atmosphere and create spectral features in thermal emission. As such, spectroscopic or multi-band emission observations can simultaneously constrain the thickness of the atmosphere and its composition (e.g., [Deming et al. 2009](#); [Whittaker et al. 2022](#)).

On the other hand, if the planet is airless, thermal emission probes surface properties, such as its mineral composition, level of roughness across multiple scales, and degree of space weathering ([Hu et al. 2012a](#); [Whittaker et al. 2022](#); [Lyu et al. 2024](#); [Tenthoff et al. 2024](#); [First et al. 2024](#)). Thus, JWST thermal emission observations provide the very first pathway towards probing exoplanet surfaces at a population level.

Under what conditions M-Earths could have atmospheres is unclear. In this context, the search for atmospheres on M-Earths can be framed as constraining the conditions in which such atmospheres can exist, and this framing has been invoked in, e.g., the Rocky Worlds DDT program ([Redfield et al. 2024](#)). Whether Solar System empirical trends in atmosphere presence/absence can be extrapolated to M stars (i.e., the ‘Cosmic Shoreline’ hypothesis, [Zahnle & Catling 2017](#)) is currently unknown, and theory suggests the harsh stellar environment of M-Earths is likely inhospitable for atmospheres (e.g., [Davenport et al. 2012](#); [Shields et al. 2016](#); [Dong et al. 2018](#) — we will discuss this point in more detail in §4). However, these simple scaling laws do not account for the possible diversity in initial volatile content of rocky worlds, which remains poorly understood. For example, there is no consensus explanation for Earth’s carbon, nitrogen, or water budget (e.g., [Kite & Schaefer 2021](#); [Li et al. 2021](#); [Hirschmann et al. 2021](#); [Krijt et al. 2022](#)), and volatile loss on rocky exoplanets is also not well-understood (e.g., [Kite & Barnett 2020](#); [Nakayama et al. 2022](#)).

Observations so far using secondary eclipses paint a murky picture for the prospect of discovering atmospheres on M-Earths. To date, no M-Earths observed in thermal emission have been revealed to conclusively have a thick atmosphere. All measured dayside temper-

atures are 1σ consistent with the no-atmosphere (‘bare rock’) limit and 2σ consistent with a perfect blackbody across a wide range of irradiation ([Kreidberg et al. 2019](#); [Crossfield et al. 2022](#); [Greene et al. 2023](#); [Zieba et al. 2023](#); [Zhang et al. 2024](#); [Xue et al. 2024](#); [Weiner Mansfield et al. 2024](#); [Wachiraphan et al. 2024](#)), or are plagued by systematics on the order of the expected eclipse depth, complicating interpretation ([August et al. 2024](#)). Moreover, molecular features have not been detected in spectral emission observations for M-Earths ([Zhang et al. 2024](#); [Xue et al. 2024](#); [Weiner Mansfield et al. 2024](#); [Wachiraphan et al. 2024](#)). However, atmospheres remain possible in some cases; e.g., TRAPPIST-1 c may have a 100 mbar Earth-like atmosphere ([Zieba et al. 2023](#); [Lincowski et al. 2023](#)) and TRAPPIST-1 b shows different brightness temperatures at 12.8 and 15 μm , possibly indicative of a thermally-inverted CO_2 -rich atmosphere ([Ducrot et al. 2023](#)).

An alternative approach to interpreting secondary eclipse depths is by examining these observations at the population level to test hypotheses that explain possible trends in the global population. For example, the Cosmic Shoreline hypothesis predicts that more massive and less irradiated exoplanets have thicker atmospheres ([Zahnle & Catling 2017](#)). Thus, homogeneously studying population-level emission data can aid in understanding controls on atmosphere presence on M-Earths.

Here, we present a tentative 1D trend in the brightness temperatures of M-Earths as a function of their irradiation temperatures. We summarize the currently available emission observations in §2 and present the trend in §3, examining a variety of atmospheric and geologic hypotheses that could explain this trend. We discuss these planets and future JWST targets in the context of the Cosmic Shoreline hypothesis in §4.

2. METHODS

2.1. Emission Observations of Rocky Planets

M-Earths observed in emission thus far span a wide range of irradiation temperatures, which we define as

$$T_{irr} = T_{\star} \sqrt{\frac{R_{\star}}{a}}, \quad (1)$$

where T_{\star} is the host star effective temperature, R_{\star} is the host star radius, and a is the planet’s orbital semi-major axis. The irradiation temperature is $\sqrt{2}$ times the equilibrium temperature of a zero-albedo planet with global heat redistribution, and it is equivalent to the substellar temperature of a tidally-locked world with zero albedo at all wavelengths (i.e., a perfect blackbody). Irradiation temperatures of observed planets range from the molten

sub-Earth GJ 367 b ($T_{irr} = 1930$ K) to the potential “Venus twin” TRAPPIST-1 c ($T_{irr} = 480$ K).

The expected disk-integrated dayside temperature of a planet can be calculated from the planet’s Bond albedo A_B and a heat redistribution factor f (Hansen 2008; Cowan & Agol 2011),

$$T_d = T_{irr} f^{1/4} (1 - A_B)^{1/4}, \quad (2)$$

where $f \rightarrow \frac{2}{3}$ for a planet with zero heat redistribution to the nightside to $f \rightarrow \frac{1}{4}$ for full heat redistribution. f is also often commonly rewritten as ε , defined as

$$f = \frac{2}{3} - \frac{5}{12} \varepsilon, \quad (3)$$

so that ε varies from 0 with no heat redistribution to 1 with full redistribution. Thus the theoretical maximum disk-integrated dayside temperature for a zero-albedo, zero-heat redistribution planet is

$$T_{d,max} = T_{irr} \left(\frac{2}{3} \right)^{1/4}. \quad (4)$$

Following recent works (Xue et al. 2024; Weiner Mansfield et al. 2024; Wachiraphan et al. 2024), we define the ‘brightness temperature ratio’ \mathcal{R} as:

$$\mathcal{R} \equiv \frac{T_d}{T_{d,max}}, \quad (5)$$

which compares the measured dayside brightness temperature to the theoretical maximum. Another useful metric is the inferred (or ‘effective’) albedo, which is the planetary Bond albedo needed to reproduce the observed dayside temperature assuming zero heat redistribution and unit emissivity and can be calculated via,

$$A_i = 1 - \mathcal{R}^4. \quad (6)$$

2.2. Determining Brightness Temperature Ratios

How are dayside temperatures determined through observations? Secondary eclipse observations can help to constrain the planet’s dayside *brightness temperature*, which is the best-fit temperature of a blackbody emitter in a given wavelength band. This value can differ slightly from the true dayside temperature, since observations do not span the full wavelength range of the planet’s thermal emission and are thus affected by wavelength-dependent gaseous molecular absorption or emissivity of the surface.

Brightness temperatures are derived from planet-to-star contrast ratios during secondary eclipse (eclipse depths) and require taking into account uncertainty in

orbital, planetary, and stellar parameters. Individual observations, however, have accomplished this by using slightly different methodology. This includes the use of spatially resolved (e.g., Zieba et al. 2023; Ducrot et al. 2023) vs. 0-D energy balance models (e.g., Xue et al. 2024; Weiner Mansfield et al. 2024), as well as fitting for per-frequency flux (e.g., Greene et al. 2023) vs. planet-to-star contrast ratios.

In this work, we combine the reported eclipse depths and uncertainties from JWST and Spitzer emission observations of TRAPPIST-1 c (Zieba et al. 2023), TRAPPIST-1 b (Greene et al. 2023; Ducrot et al. 2023), LTT 1445 A b (Wachiraphan et al. 2024), GJ 1132 b (Xue et al. 2024), GJ 486 b (Weiner Mansfield et al. 2024), LHS 3844 b (Kreidberg et al. 2019), GJ 1252 b (Crossfield et al. 2022), and GJ 367 b (Zhang et al. 2024) to homogeneously re-derive dayside brightness temperature ratios. These observations utilize four instruments that have different wavelength coverage, including: the Spitzer Infrared Array Camera (IRAC, Fazio et al. 2004) Channel 2 (4 – 5 μm), JWST MIRI (Rieke et al. 2015) Low-Resolution Spectrometer (LRS, 5 – 12 μm), and MIRI imaging filters F1280W (11.6 – 14.0 μm) and F1500W (13.5 – 16.5 μm).

To remove potential biases and avoid differences in modeling schemes used in deriving brightness temperature ratios, we use a nested sampling approach (with *dynesty*, Speagle 2020) that takes into account uncertainties in stellar effective temperature, stellar surface gravity [$\log(g)$], stellar metallicity ([M]), as well as the orbital semi-major axis to stellar radius ratio (a/R_\star) and planet-to-star radius ratio (R_p/R_\star). These parameters are shown in Table 1. Following Xue et al. (2024), the broadband planet-to-star flux ratio (F_p/F_\star) is determined assuming an isothermal blackbody emitter for the planet,

$$\frac{F_p}{F_\star} = \left(\frac{R_p}{R_\star} \right)^2 \times \frac{\int \frac{\pi B_\lambda(\mathcal{R} \times T_{d,max}(T_\star, a/R_\star))}{hc/\lambda} W_{inst,\lambda} d\lambda}{\int \frac{M_\lambda(T_\star, \log(g), [M])}{hc/\lambda} W_{inst,\lambda} d\lambda}, \quad (7)$$

where B_λ is the Planck function and M_λ is the model stellar flux. $W_{inst,\lambda}$ is the throughput function for each instrument, which we determine from *Pandemia* 4.0 (Pontoppidan et al. 2016). After integrating over the instrument bandpass, the residual of this value (compared to the reported eclipse depth) is then used to calculate the log evidence during nested sampling, which gives a posterior distribution for the brightness temperature ratio \mathcal{R} .

The choice of stellar model has a large impact on the modeled emission spectra of rocky planets. Stellar mod-

Table 1. Host Star and System Parameters Used in Brightness Temperature Nested Sampling

Star	T_\star (K)	$\log(g[cm/s^2])$	[M/H]	a/R_\star	R_p/R_\star
TRAPPIST-1 c	2566 ± 26	$5.2395^{+0.0073}_{-0.0056}$	0.0530 ± 0.0880	$28.549^{+0.212}_{-0.129}$	0.08440 ± 0.00038
TRAPPIST-1 b	2566 ± 26	$5.2395^{+0.0073}_{-0.0056}$	0.0530 ± 0.0880	20.83 ± 0.155	0.08590 ± 0.00037
LTT 1445 A b	3340 ± 150	$4.982^{+0.040}_{-0.065}$	-0.34 ± 0.09	30.2 ± 1.7	0.0454 ± 0.0012
GJ 1132 b	3229^{+78}_{-62}	$5.037^{+0.034}_{-0.026}$	-0.17 ± 0.15	$15.26^{+0.59}_{-0.45}$	0.04943 ± 0.00015
GJ 486 b	3317^{+36}_{-37}	$4.9111^{+0.0068}_{-0.0110}$	$-0.15^{+0.13}_{-0.12}$	$11.380^{+0.074}_{-0.150}$	$0.037244^{+0.000059}_{-0.000056}$
LHS 3844 b	3036 ± 77	5.06 ± 0.01	0 ± 0.5^a	7.109 ± 0.029	0.0635 ± 0.0009
GJ 1252 b	3458 ± 157	4.83497 ± 0.00292	0.1 ± 0.1	5.03 ± 0.27	0.0277 ± 0.0011
GJ 367 b	3522 ± 70	4.776 ± 0.026	-0.01 ± 0.12	3.410 ± 0.065	0.01399 ± 0.00028

NOTE—Stellar and system parameters used for nested sampling, in order of irradiation temperature. Values are taken from: TRAPPIST-1 c/b (Agol et al. 2021), LTT 1445 A b (Wachiraphan et al. 2024), GJ 1132 b (Xue et al. 2024), GJ 486 b (Weiner Mansfield et al. 2024), LHS 3844 b (Vanderspek et al. 2019), GJ 1252 b (Crossfield et al. 2022), and GJ 367 b (Goffo et al. 2023).^aThis value has not been measured and we assume a relatively unconstrained prior.

els are not perfect and often conflict with observed stellar spectra, and as estimates of \mathcal{R} inherently require accurate stellar models, this can lead to inaccuracies in the interpretation of eclipse spectra. However, many observations have used a single stellar model to interpret eclipse data (e.g., Kreidberg et al. 2019; Greene et al. 2023; Zieba et al. 2023). Here, we use both the SPHINX M-dwarf Spectral Grid (Iyer et al. 2023, updated May 30 2024), which has been extensively vetted through observations of M dwarfs, and PHOENIX stellar models (Husser et al. 2013). Brightness temperature ratios can vary significantly between the two models (up to $\sim 4\%$ or $\sim 1\sigma$), highlighting the importance of accounting for uncertainties in stellar modeling. For nested sampling, we use a linear interpolation scheme for both SPHINX¹ and PHOENIX (using `pysynphot`, STScI Development Team 2013) to estimate model spectra between grid points.

2.2.1. Broadband Versus Spectral Fitting for Determining Brightness Temperatures

Four of the eight planets analyzed in this study use MIRI LRS data, which involves an additional uncertainty that we now discuss. With MIRI LRS, it is possible to retrieve wavelength-resolved eclipse depths (eclipse spectra), giving information on possible atmospheric and surface spectral features while simultaneously constraining the dayside temperature. Assuming a blackbody, such spectra can be fitted in F_p/F_\star vs. wavelength space to find the best-fit blackbody temperature.

¹ <https://github.com/ideasrule/sphinx>

On the other hand, early observations suggest that using broadband ‘white light’ curves may be more effective at minimizing the effects of systematics and red noise, leading to more robust *bandpass-integrated* eclipse depths. However, the systematic ramps of LRS are likely wavelength-dependent (Zhang et al. 2024; Xue et al. 2024; Weiner Mansfield et al. 2024), and the ‘white light’ approach cannot account for such effects.

Despite using the same fundamental data, these techniques yield different values for \mathcal{R} . For GJ 486 b, fitting the spectrum lowers the derived \mathcal{R} value by $\sim 6\%$ ($\sim 3\sigma$) when compared to white light, greatly affecting interpretation of the data. We find that a synthetic reconstruction of the white light eclipse depth using the eclipse spectrum is also lower than the observed white light eclipse depth for GJ 1132 b and GJ 367 b. Future M-Earth observations with LRS will be needed to better understand the impact of wavelength-dependent systematics on derived brightness temperatures, as this may serve as an additional false positive for atmosphere detection.

In this work, we adopt the re-derived brightness temperature ratios using ‘white light’ broadband LRS eclipse depths, although we report values from spectral fitting as well. For spectral fits, our nested sampling algorithm uses the same methodology as Eq. 7, but over multiple wavelength bins simultaneously. For these fits, we use the fiducial LRS emission spectra reported in Zhang et al. (2024); Xue et al. (2024); Weiner Mansfield et al. (2024); Wachiraphan et al. (2024). Our homogeneously re-derived brightness temperature ratios are shown in Table 2, and are consistent with those derived in the original observations.

Table 2. Planet Parameters and Homogeneously-Derived \mathcal{R} Values Used in This Study

Planet	T_{irr} (K)	Eclipse Depth(s) (ppm)	\mathcal{R}		Instrument(s)	M_p (M_{\oplus})	R_p (R_{\oplus})
			SPHINX	PHOENIX			
TRAPPIST-1 c	480 ± 5	421 ± 94	$0.877^{+0.073}_{-0.075}$	$0.903^{+0.075}_{-0.082}$	MIRI F1500W	1.31 ± 0.06	1.10 ± 0.01
TRAPPIST-1 b ^a	562 ± 5	$452 \pm 86, 775 \pm 90$	$0.910^{+0.037}_{-0.036}$	$0.933^{+0.039}_{-0.040}$	MIRI F1280W, F1500W	1.37 ± 0.07	1.12 ± 0.01
Greene+23		861 ± 99	$0.993^{+0.049}_{-0.052}$	$1.021^{+0.054}_{-0.055}$	F1500W		
LTT 1445 A b	600 ± 30	41 ± 9	$0.950^{+0.063}_{-0.071}$	$0.955^{+0.066}_{-0.072}$	MIRI LRS	2.7 ± 0.2	1.3 ± 0.1
Spectral Fit			$0.948^{+0.043}_{-0.043}$	$0.954^{+0.048}_{-0.046}$			
GJ 1132 b	826 ± 14	140 ± 17	$0.940^{+0.043}_{-0.040}$	$0.952^{+0.042}_{-0.044}$	MIRI LRS	1.84 ± 0.19	1.19 ± 0.04
Spectral Fit			$0.902^{+0.038}_{-0.038}$	$0.914^{+0.038}_{-0.038}$			
GJ 486 b	985 ± 10	135.5 ± 4.9	$0.992^{+0.017}_{-0.017}$	$0.981^{+0.017}_{-0.018}$	MIRI LRS	2.77 ± 0.07	1.29 ± 0.02
Spectral Fit			$0.935^{+0.015}_{-0.015}$	$0.926^{+0.015}_{-0.016}$			
LHS 3844 b	1138 ± 28	380 ± 40	$0.996^{+0.033}_{-0.034}$	$1.002^{+0.033}_{-0.034}$	IRAC Channel 2	2.2 ± 1.0^b	1.30 ± 0.02
GJ 1252 b	1540 ± 98	149^{+25}_{-32}	$1.067^{+0.094}_{-0.105}$	$1.035^{+0.090}_{-0.103}$	IRAC Channel 2	1.32 ± 0.28	1.18 ± 0.08
GJ 367 b	1930 ± 45	79 ± 4	$1.076^{+0.047}_{-0.045}$	$1.035^{+0.040}_{-0.037}$	MIRI LRS	0.63 ± 0.05	0.70 ± 0.02
Spectral Fit			$1.002^{+0.046}_{-0.045}$	$0.967^{+0.042}_{-0.038}$			

NOTE—LHS 1478 b data are not included in our sample due to issues discussed in Appendix §A.2. Planetary parameters and eclipse depths are from: TRAPPIST-1 c (Agol et al. 2021; Zieba et al. 2023), TRAPPIST-1 b (Agol et al. 2021; Greene et al. 2023; Ducrot et al. 2023), LTT 1445 A b (Wachiraphan et al. 2024), LHS 3844 b (Vanderspek et al. 2019; Kreidberg et al. 2019), GJ 1132 b (Xue et al. 2024), GJ 486 b (Weiner Mansfield et al. 2024), GJ 1252 b (Shporer et al. 2020; Crossfield et al. 2022), and GJ 367 b (Goffo et al. 2023; Zhang et al. 2024). ^aSee Appendix §A.1 for a discussion of TRAPPIST-1 b data used in this study. ^bLHS 3844 b does not have a measured mass and we adopt the unconstrained value assumed in Diamond-Lowe et al. (2021).

backscattered towards the observer (reflected light), ignoring the opposition surge effect:

2.3. Surface Modeling

To estimate the effects of surface compositions on brightness temperatures, we largely follow the simplified 0-D energy balance model of Mansfield et al. (2019). Diverging from Mansfield et al. (2019), we use the approximations presented in the Hapke (2012) scattering model and single scattering albedo (w) data derived in Hu et al. (2012a) to determine the spherical reflectance r_s (equivalent to spherical albedo in an isotropic scatterer):

$$r_s(\lambda) = r_0(\lambda) \left(1 - \frac{1 - r_0(\lambda)}{6} \right), \quad (8)$$

where r_0 is the ‘diffusive reflectance’:

$$r_0(\lambda) = \frac{1 - \sqrt{1 - w(\lambda)}}{1 + \sqrt{1 - w(\lambda)}}. \quad (9)$$

Hemispherical emissivity ε_h is determined via,

$$\varepsilon_h(\lambda) = 1 - r_s(\lambda). \quad (10)$$

Similarly, we use the Hapke (2012) model to derive the geometric albedo A_g , which controls the amount of light

$$A_g(\lambda) = 0.49r_0(\lambda) + 0.196r_0^2(\lambda). \quad (11)$$

The strength of the opposition surge effect is highly dependent on the surface material composition and grain size (e.g., Jost et al. 2016) and it not calculable *a priori*. Regardless, it has little effect on the emission spectrum due to being a reflected light phenomenon. We note that the distinction between spherical (wavelength-dependent Bond) albedo and geometric albedo was erroneously not made in Mansfield et al. (2019), and discuss implications in §4.2.

3. RESULTS

3.1. Trend in Brightness Temperature Ratio with Irradiation Temperature

We compare our homogeneously re-derived SPHINX dayside brightness temperatures ratios (Table 2) as a function of irradiation temperature in Fig. 1. While all individual observations are consistent with a no thick atmosphere null hypothesis, together these results show a trend in brightness temperature as a function of irradiation temperature; \mathcal{R} decreases with colder temperatures.

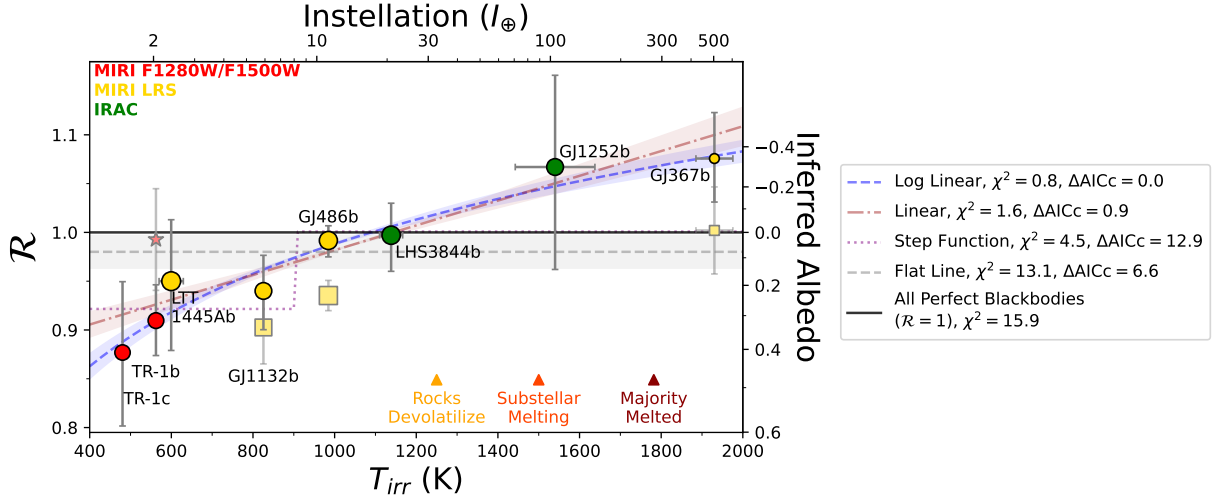


Figure 1. Our homogeneously-derived brightness temperature ratios \mathcal{R} (the measured dayside brightness temperature compared that of a perfect blackbody) using SPHINX stellar models as a function of irradiation temperature for M-Earths with emission data (Table 2). Point radii are proportional to planet radii. There is an apparent trend in brightness temperature as a function of irradiation temperature; \mathcal{R} decreases with colder temperatures. We include chi-square statistic χ^2 and ΔAICc (corrected Akaike Information Criterion) for five possible simple functions describing the observed data, noting that a trend is strongly favored over a flat line. ‘White light’ broadband data (values used in our study) are shown as circles, whereas fits to spectra are shown in squares. The star represents TRAPPIST-1 b F1500W data originally presented in [Greene et al. \(2023\)](#) not used in this study (see Appendix §A.1). Rocky surfaces of composition similar to Earth’s are expected to largely devolatilize around ~ 1250 K and completely melt by 1500 K ([Lutgens et al. 2000](#); [Mansfield et al. 2019](#)).

To statistically evaluate this trend, we use both goodness-of-fit hypothesis testing and model comparison based on information-theory criteria. We adopt the ‘flat line’ (i.e., no trend) model as our null hypothesis to compare to two simple linear models with Student’s t -tests. These linear models consist of a standard linear regression,

$$\mathcal{R} = \alpha_0 + \alpha_1 T_{irr}, \quad (12)$$

with weighted least-squares fit coefficients of $\alpha_0 = 0.8458 \pm 0.0208$ and $\alpha_1 = 0.000127 \pm 0.000020$, and a ‘log-linear’ regression,

$$\mathcal{R} = \beta_0 + \beta_1 \ln(T_{irr}), \quad (13)$$

with coefficients $\beta_0 = 0.0424 \pm 0.1001$, $\beta_1 = 0.1369 \pm 0.0146$. Through t -tests, we reject the null hypotheses that $\alpha_1 = 0$ or $\beta_1 = 0$ (i.e., no trend) at p -values of 7.3×10^{-4} (3.4σ) and 8.3×10^{-5} (3.9σ), respectively.

To further compare various simple models, we calculate the chi-square statistic (χ^2), relative corrected Akaike Information Criterion (AICc), and Bayesian Information Criterion (BIC) values, shown in Table 3. AICc is specifically used for small sample sizes by penalizing more complex models ([Anderson & Burnham 2002](#)). According to all of our metrics, the log-linear description of the data is favored over the null hypothesis. The log-linear model finds the best AICc, with a $\Delta\text{AICc} = 6.6$ over the flat line model, which implies

‘considerably less’ support for the latter ([Anderson & Burnham 2002](#)). The ΔBIC value (10.2) also surpasses the threshold indicating ‘very strong evidence’ in favor of the log-linear model ($\Delta\text{BIC} = 10$, [Raftery 1995](#)), although this value may be overly optimistic for our small sample size. This trend suggests a T_{irr} -dependent process(es) that alters the inferred albedo of colder planets.

However, nested sampling using PHOENIX stellar models tend to push \mathcal{R} towards unity (Table 2, also see Appendix Fig. B1). In this case, the evidence for a trend, described by the relation

$$\mathcal{R} = (0.3685 \pm 0.0679) + (0.0886 \pm 0.0099) \times \ln(T_{irr}) \quad (14)$$

is much weaker. While we still reject the null hypotheses that $\alpha_1 = 0$ or $\beta_1 = 0$ with p -values of 8.6×10^{-4} (3.3σ) and 1.1×10^{-4} (3.9σ), respectively, ΔAICc suggests that the flat line, linear, and log-linear models are roughly equally as likely. Thus, while SPHINX (which is a stellar grid specifically dedicated for the low-mass stars in this study) fitting shows strong evidence for a trend in \mathcal{R} , we emphasize that this is a tentative identification that requires more data or more precise stellar modeling to further support.

3.2. Effects of Surface Composition on Brightness Temperature

Table 3. Statistics of Simple Functions Describing the Data

Function	$\chi^2 (N = 8)$	ΔAICc	ΔBIC
SPHINX Data			
Log-Linear	0.8	0	0
Linear	1.7	0.9	0.9
Flat Line	13.1	6.6	10.2
Step Function	4.5	12.9	5.6
All Perfect Blackbodies ($\mathcal{R} = 1$)	15.9	-	-
PHOENIX Data			
Log-Linear	0.4	0	0
Linear	0.8	0.4	0.4
Flat Line	6.1	-0.1	3.4
Step Function	2.6	11.2	4.0
All Perfect Blackbodies ($\mathcal{R} = 1$)	9.4	-	-

All planets in this study lack evidence for a thick atmosphere. In the absence of an atmosphere, infrared emission observations probe the composition of rocky exoplanet surfaces. Here, we explore possible *geophysical* processes that could explain a trend in \mathcal{R} , making hotter solid surfaces darker.

3.2.1. Space Weathering

Space weathering is a generalized term that refers to surface alteration by stellar winds and micrometeorite impacts. The surfaces of Mercury and the Moon are darker than pulverized rocks of similar composition (Hapke 2001), having low estimated Bond albedos of 0.06 and 0.13, respectively (Mallama et al. 2002; Matthews 2008). This darkening is also important for asteroids (e.g., Chapman 2004; Pieters & Noble 2016). Darkening occurs primarily from the conversion of Fe locked in silicates on the surface to nm-sized nanophase metallic Fe (npFe⁰) and larger-grained microphase Fe (mpFe⁰). These particles darken a thin surface layer, lowering planet albedo. In the case of an Fe-poor, carbon-rich surface such as that of Mercury (Pieters & Noble 2016), darkening is thought to be due to graphite, possibly a relict of a graphite flotation crust (Keppler & Golabek 2019). Space weathering can either redden rock spectra by reducing albedo primarily in the visible-NIR for npFe⁰, or reduce albedo over all wavelengths in the case of mpFe⁰ or graphite-coating (Pieters & Noble 2016). Space weathering can be prevented by even thin, Mars-like atmosphere.

Most previous theoretical studies of exoplanet surfaces (e.g., Hu et al. 2012a; Mansfield et al. 2019; Whittaker et al. 2022; Hammond et al. 2024) model the emission

spectra of *fresh*, unweathered regolith and thus likely overestimate the impact of composition on brightness temperature for space-weathered planets. The insolation dependence of space weathering is not well understood. Zieba et al. (2023) use stellar wind strength scaling to estimate a *space weathering timescale* for TRAPPIST-1 c (the least irradiated planet considered here) of $10^2 - 10^3$ yr, compared to $10^5 - 10^7$ yr for the Moon (according to Hapke 1977). If this is correct, airless M-Earths would have to experience dayside resurfacing through volcanism on very short timescales to produce detectable nonzero surface albedo. Indeed, the Spitzer phase curve of LHS 3844 b has suggested that it is highly space weathered (Lyu et al. 2024). If space weathering is efficient and atmospheres are lacking on M-Earths then very low-albedo surfaces are likely on these planets.

To quantify the effects of space weathering on measured brightness temperatures, we simulate the effects of the mixture of a host material and npFe⁰ or graphite absorbing particles, following Hapke (2001) and Lyu et al. (2024), using single scattering albedo profiles from Hu et al. (2012a). Lyu et al. (2024) find that the phase curve of LHS 3844 b is most consistent with either mixtures of either 5 wt% npFe⁰ or 5 wt% graphite. They consider 5% an upper limit given the ~ 5 wt% Fe crustal content of the Earth and the Moon (Lucey et al. 1995; Taylor & McLennan 2001; Taylor et al. 2006). This is noticeably higher than contamination in lunar soil samples, which suggest $\sim 0.1 - 0.5$ wt% npFe⁰ (Hapke 2001; Noble et al. 2007), further supporting efficient space weathering for M-Earths.

Due to uncertainties in the exact behavior of space weathering around M stars, we test the effects of both weak Moon-like (0.3 wt% npFe⁰ or graphite) and stronger LHS 3844 b-like (5 wt%) space weathering on the albedo profiles of Hu et al. (2012a). We simulate MIRI LRS emission observations for a wide range of T_{irr} and surface types. We find (Fig. 2) that universal LHS 3844 b-like highly space weathered surfaces, predicted by stellar wind scaling arguments, *cannot* explain a trend in brightness temperature alone, as strong space weathering pushes \mathcal{R} very close to unity. However, if space weathering is much weaker for rocky planets around M-stars than inferred in Zieba et al. (2023), moderate-albedo surfaces (e.g., fresh basalts or ultramafic grains) that are more space-weathered on close-in planets are a possible explanation for the observed trend.

3.2.2. Regolith Grain Size

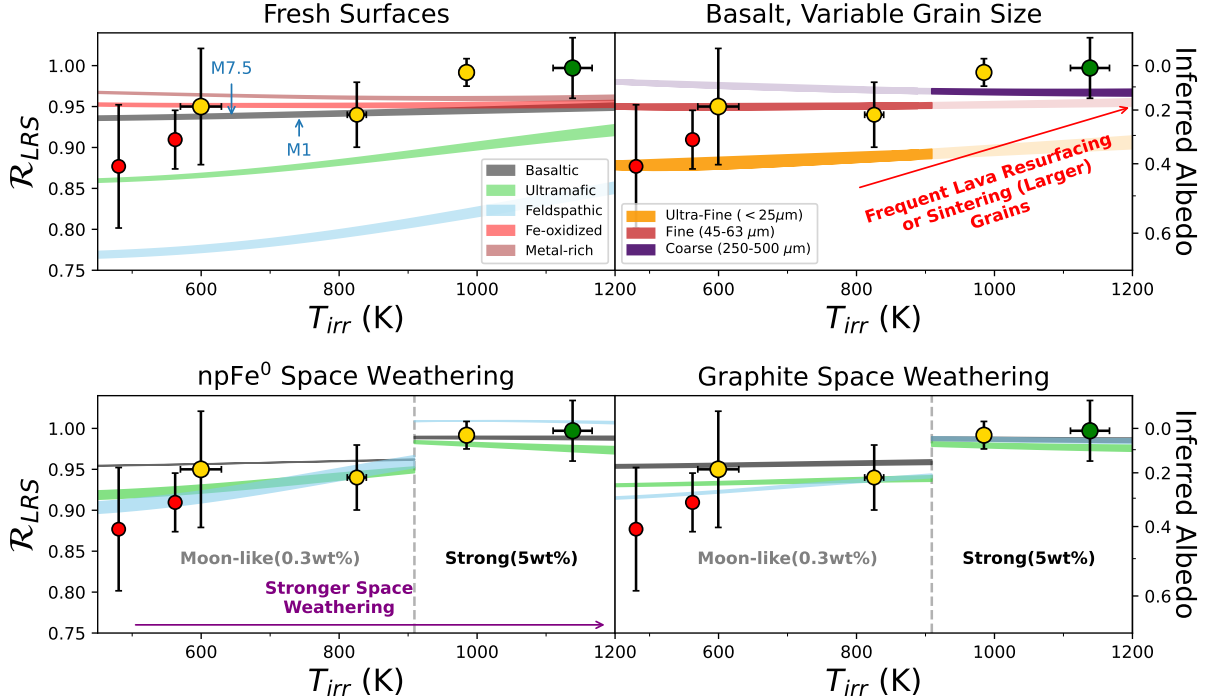


Figure 2. Simulated effects of ‘bare-rock’ fresh surface albedo profiles from Hu et al. (2012a), varying regolith grain sizes of basalt, and npFe⁰/graphite space weathering on simulated emission observations in the MIRI LRS bandpass (5 – 12 μm). Brightness temperature ratios in the MIRI F1500W and Spitzer IRAC2 bandpasses show similar trends. Planets too hot for solid surfaces ($T_{irr} \gtrsim 1250$ K) are not shown. Results are dependent on the exact stellar properties, and we include results for a GJ 367-like M1 star and a TRAPPIST-1-like M7.5 star as bounding cases defining the width of each colored band. This roughly encompasses the spread expected for M-Earths. A trend of increasing brightness temperature ratio (\mathcal{R}) with irradiation temperature (T_{irr}) can be explained by grain sizes increasing with temperature or stronger space weathering on closer-in planets, as explored in §3.2.

The albedo profiles used in previous surface studies (Hu et al. 2012a; Mansfield et al. 2019; Lyu et al. 2024) assume a fine-grained regolith formed by long-term weathering of surface rock. However, grains can be coarsened by solid-state deformation when close to the melting point (sintering, e.g., Mergny & Schmidt 2024), or by volcanic resurfacing.

Larger grain sizes decrease visible and near-infrared reflectance of particulate regolith (e.g., Zaini et al. 2012; Zhuang et al. 2023), both decreasing Bond albedo and the magnitude of spectral features. Lunar regolith is considered fine-grained, with bulk optical properties dominated by particles $\sim 10 - 45 \mu\text{m}$ in size (Fischer & Pieters 1994). However, closer-in planets may experience faster volcanic resurfacing (Jackson et al. 2008). To form the fine-grained regolith that is assumed in the albedo profiles of Hu et al. (2012a) and subsequent works requires long-term weathering that may be reset by lava resurfacing or by high temperature sintering. Basaltic rock begins forming melt glass around ~ 1250 K (Winter 2014), and thus sintering may be important on hotter

worlds like GJ 486 b and LHS 3844 b which are near this melting point.

To estimate the effects of grain size on \mathcal{R} , we use results from the RELAB Spectral Database². Particulate of the basalt sample 79-3b (the same sample used in the ‘basaltic’ albedo profile of Hu et al. 2012a) were crushed and sorted via particle size bins, ranging from $< 25 \mu\text{m}$ to $500 \mu\text{m}$ (PI: John F. Mustard). Measured bidirectional reflectance values cover the $0.3 - 25.0 \mu\text{m}$ wavelength range. These data were converted to single scattering albedo, spherical reflectance, and hemispherical emissivity values following methods in Hapke (2012). Results (Fig. 2) confirm that grain size can have a significant impact on \mathcal{R} , with larger grain sizes leading to universally hotter planets for the same underlying material. Thus, if hotter planets have higher resurfacing rates and correspondingly coarser surfaces, this can explain a 1-D trend in brightness temperatures.

² <https://sites.brown.edu/relab/relab-spectral-database/>

We discuss a variety of other processes that can significantly affect \mathcal{R} but would likely *not* impart a trend with irradiation temperature in Appendix B. This includes tidal interactions, surface roughness, and Titan-like haze formation.

3.3. Wavelength-Dependent Effects of Atmospheres on \mathcal{R}

While our sample of planets lack evidence for *thick* atmospheres, we cannot rule out thin/tenuous atmospheres because some models predict that volcanic outgassing or volatile replenishment via cometary impacts outpaces atmospheric loss after a \sim Gyr, reviving the atmosphere (e.g., Kral et al. 2018; Kite & Barnett 2020). Such revival would be easiest on colder planets. To test the effects that an onset of thin atmospheres would have on observed \mathcal{R} values, we forward model possible atmospheres for each target, varying the surface pressure and composition, similar to work done in Whittaker et al. (2022); Ih et al. (2023); Xue et al. (2024); Weiner Mansfield et al. (2024). For each system, we use SPHINX stellar models to calculate the stellar spectrum and use the radiative-convective equilibrium code HELIOS (Malik et al. 2017, 2019) to calculate the 1D thermal structure and emission spectrum of the planet. HELIOS employs the scaling relationship developed in Koll (2022) to calculate the heat redistribution given the surface pressure, equilibrium temperature, and opacity of the atmosphere. We model the atmosphere for surface pressures from 10^{-4} - 10^2 bar in 1-dex intervals and for Earth-like (1% H₂O, 400 ppm CO₂) and Venus-like (96.5% CO₂, 150 ppm SO₂, 20 ppm H₂O) compositions (Olson et al. 2018; Marcq et al. 2018). We assume a blackbody at the surface. These forward models are calculated for each planet/star pair based on parameters in Table 1. We use the bandpass of each instrument weighted by the stellar spectrum to calculate the binned eclipse depth, as done in Whittaker et al. (2022); Ih et al. (2023).

We show the brightness temperature ratios \mathcal{R} in each instrument bandpass in Fig. 3, for surface pressures corresponding roughly to Venus-, Earth-, and Mars-like surface pressures in 2-dex intervals. Here, a clear trend in possible atmospheric thickness is tricky to infer because the instrument choice can have a large effect, with bandpasses that target specific bands, e.g., IRAC Channel 2 or MIRI F1500W for CO₂ being the most discerning. However, when viewed in consistent surface pressure space (Fig. 4) upper limits on surface pressure become somewhat larger for colder planets, possibly indicative of the onset of thin atmospheres. Planets hotter than $T_{\text{irr}} \sim 1000$ K are difficult to reconcile with even thin CO₂-rich atmospheres.

It is worth considering whether these thin atmospheres are sustainable. Some models predict that atmospheres on M-Earths would require extremely high volcanic outgassing fluxes to balance high thermal escape rates (e.g., Diamond-Lowe et al. 2021; Crossfield et al. 2022; Krissansen-Totton 2023; Diamond-Lowe et al. 2024). However, protective magnetic fields (Segura et al. 2010; Luo et al. 2024), cooling of atmospheres by radiative recombination and atomic line cooling (Nakayama et al. 2022), and/or potentially high initial volatile inventories (Bergin et al. 2023; Peng & Valencia 2024), could allow M-Earths to retain atmospheres. Outer, colder M-Earths are more likely to retain some atmosphere because they experience far less atmospheric loss fluxes from processes like thermal escape, solar wind stripping, and impact-based erosion (e.g., Ribas et al. 2016; Dong et al. 2018; Kite & Barnett 2020).

Instruments included in this study offer tradeoffs between the efficiency of atmosphere detection and observability of targets. MIRI F1500W can offer efficiently ruling out atmospheres with even a small amount of CO₂, but may be sensitive to false positives due to the limited wavelength coverage (Hammond et al. 2024). False negatives due to thermally-inverted atmospheres have also been suggested for F1500W (Ducrot et al. 2023, also see Appendix §B.4).

On the other hand, MIRI LRS offers the most precise constraints on planetary dayside *effective* temperature and is simultaneously sensitive to select gaseous spectral features, the effects of heat redistribution, and possibly surface mineralogy (e.g., Whittaker et al. 2022; First et al. 2024). However, detailed characterization incorporating spectral information may only be suitable for very observationally favorable (and hot) targets unlikely to host atmospheres due to low eclipse depths in the MIRI LRS wavelength range for colder targets. Studying population-level effects of the onset of thin atmospheres should ideally use the same instrument(s), since as shown in Fig. 3, the chosen instrument has a large effect on \mathcal{R} .

A caveat to our atmosphere analyses is that we assume blackbodies at the surface. Medium to high albedo surfaces on planets with even thin atmospheres are more likely than airless bodies as they are not subject to space weathering, and may modify the planet’s energy budget and subsequently \mathcal{R} .

4. DISCUSSION

4.1. Cosmic Shoreline Hypothesis

The Cosmic Shoreline hypothesis posits that whether Solar System bodies are able to retain significant atmospheres or not is controlled by atmospheric escape pro-

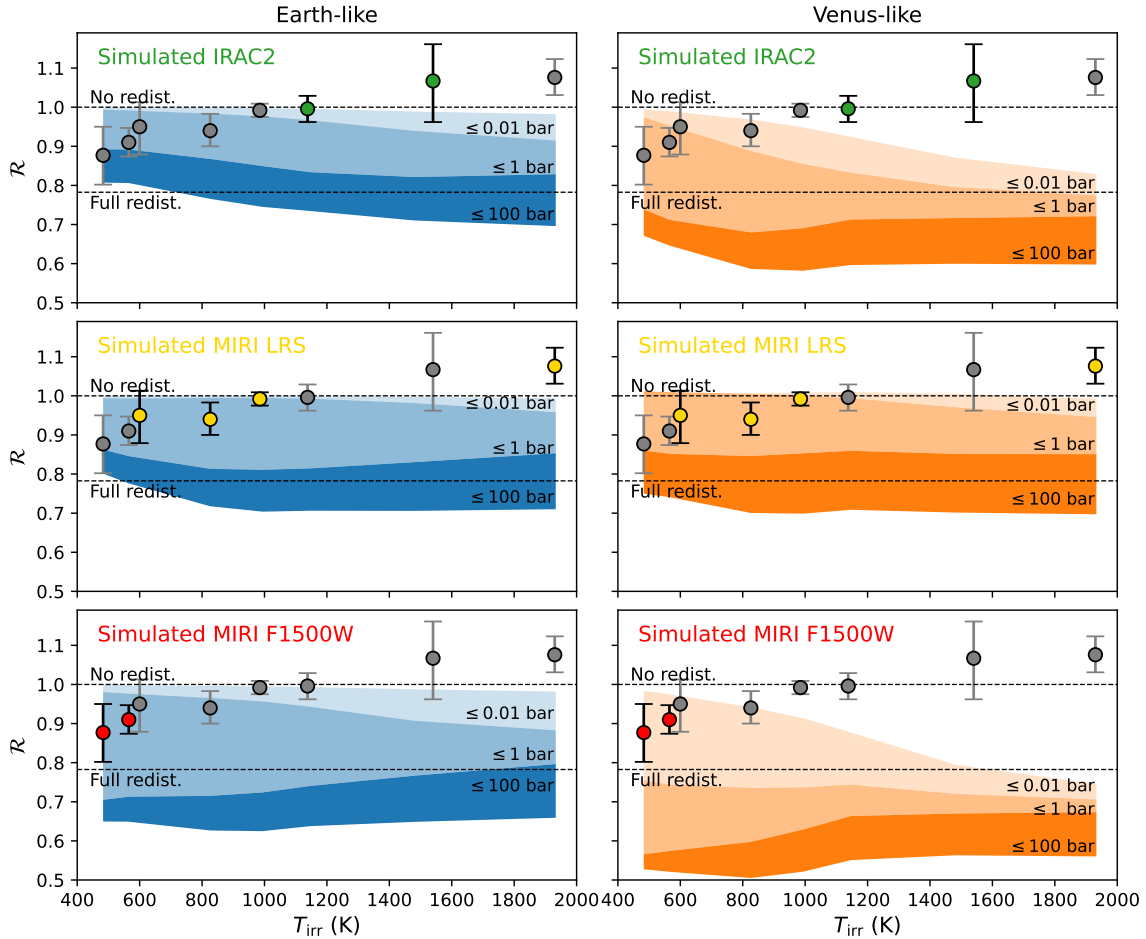


Figure 3. The calculated brightness temperature ratio (\mathcal{R}) for each target from atmospheric forward models varying surface pressures, plotted against irradiation temperature. Each row shows the brightness temperatures calculated in the bandpass of IRAC Channel 2, MIRI LRS, and MIRI F1500W, respectively. Observations using the respective instrument are highlighted in each panel. The bottom of each contour corresponds to roughly Mars-like (0.01 bar), Earth-like (1 bar), and Venus-like (100 bar) surface pressures. The brightness temperature ratio corresponding to an absorber-less atmosphere with no redistribution and full redistribution are shown as dashed lines.

cesses, not initial volatile endowment: “nurture”, not “nature” (Zahnle & Catling 2017). It is still unclear which of X-ray and Extreme Ultraviolet (XUV) radiation, bolometric instellation (radiation over all wavelengths), or high-energy impactors is the main control on atmospheric loss for Earth-sized planets (Schlichting & Mukhopadhyay 2018; Wyatt et al. 2020; King & Wheatley 2021).

M-Earths endure very high XUV flux, especially in the pre-saturation phase of their host stars, though stellar activity that can drive atmospheric loss continues for many gigayears into the main sequence (King & Wheatley 2021). In addition, their close-in orbits subject them to high-energy impactors, further promoting atmospheric loss (Wyatt et al. 2020). However, late-stage impactors, especially for colder M-Earths, might

replenish atmospheres depreciated by XUV and high-energy impacts (Kral et al. 2018).

In Fig. 5, we show our sample of planets in the context of these three loss mechanisms alongside Solar System planets. These results suggest that these planets are not expected to be able to retain significant atmospheres from multiple atmospheric loss standpoints, consistent with their measured near blackbody-like \mathcal{R} values.

However, the solar system is unusual [e.g., most exoplanetary systems lack a Jupiter analog (Fernandes et al. 2019), and the occurrence rate is even lower for the M-type stars considered in this study (Montet et al. 2014)], so the reliance of these three scaled approaches on Solar System data introduces major uncertainty. As Zahnle & Catling (2017) write, “we do not know if the shoreline is broad or narrow (i.e., whether the transition from a thin atmosphere to an atmosphere too thick and deep

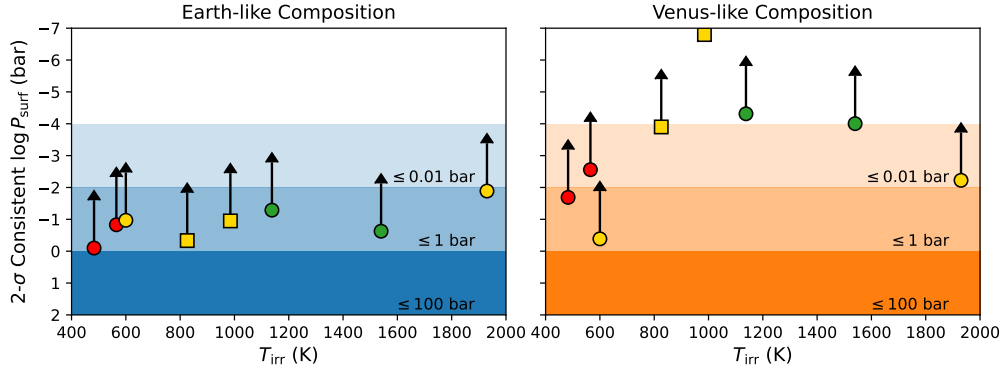


Figure 4. The maximum surface pressure consistent with each observation at 2σ as per Fig. 3, accounting for each instrument. Here, the consistent surface pressures are calculated using measured eclipse depths and their uncertainties (rather than \mathcal{R}). The square points indicate that the spectral information available from LRS was used to find the constraint, where the consistent surface pressures are calculated using goodness-of-fit of the binned eclipse spectra. The TRAPPIST-1 b point takes both F1280W and F1500W observations into account.

to be habitable to an ecology like our own is gentle or abrupt), nor in which ways our solar system is representative or unrepresentative of extrasolar systems.” Fig. 5 also does not consider processes that can replenish volatiles over long timescales [e.g., late-stage prolonged outgassing (Kite & Barnett 2020) or cometary impacts (Kral et al. 2018)]. Thus, more data are needed to test if the tendency for planets closer to the Shoreline to generally show higher inferred albedo corresponds to a Cosmic Shoreline, or something else.

4.2. Can Reflective Bare-Rock Surfaces be False Positives for Atmospheres?

Mansfield et al. (2019) argue that for warm ($400\text{ K} < T_{\text{irr}} < 1250\text{ K}$) rocky planets, bare rock surfaces (originally presented in Hu et al. 2012a) are unlikely to serve as false positives for atmosphere detection. However, the energy balance model of Mansfield et al. (2019) does not distinguish between geometric and spherical albedo, leading to estimated planetary Bond albedos that range from $\sim 70\%$ to $\sim 100\%$ that of the true value.

Geometric albedo refers to the fraction of light reflected (and emitted) towards the observer when compared to a perfect Lambertian disk. This value is fundamentally different from the *spherical* albedo, which describes the total fraction of incoming light scattered in all directions. The Bond albedo, and subsequently the amount of radiation absorbed by the planet, is determined by integrating the spherical albedo over the incoming stellar spectrum. Hemispherical emissivity is also determined via the spherical albedo. These quantities are all fundamentally computed from the single scattering albedo of the material, which we use in this work (§2.3). An explicit comparison of albedo profiles

used in this study and those used in Mansfield et al. (2019) is shown in Fig. 6

The increased albedos used in our model cool the planet, leading to higher values of inferred albedo for most bare rock surfaces than presented in Mansfield et al. (2019). This effect is also noticeable in the recent work of Hammond et al. (2024), who derive relatively high (> 0.34) Bond albedos for a wide variety of plausible surface types from the RELAB spectral database.

For some surface types, this cooling effect can be comparable to the heat redistribution expected of thick atmospheres. For TRAPPIST-1, our derived Bond albedos for the surface profiles from Hu et al. (2012a) are as follows: metal-rich - 0.13, Fe-oxidized - 0.20, basaltic - 0.24, ultramafic - 0.49, feldspathic - 0.67, clay - 0.67, and granitoid - 0.69. Inferred albedos in the LRS band-pass are similarly high (Fig. 2). The inferred albedo of some of these surfaces is comparable to the cooling expected of full heat redistribution for a thick atmosphere ($A_i = 0.63, \mathcal{R} = 0.78$). This would suggest that high albedo of exotic surface types not seen in the Solar System (in the absence of space weathering) may serve as false positives for atmospheric heat redistribution. This was also recently highlighted by Hammond et al. (2024).

However, the effect of surface composition on the Bond albedo of airless planets is likely overestimated by the albedo profiles of Hu et al. (2012a). Mercury and the Moon have low Bond albedos of 0.06 and 0.13, respectively, despite having fine-grained, largely basaltic regolith (Mallama et al. 2002; Matthews 2008). The discrepancy between theoretical and observed albedos is due to space weathering on the outermost layer of the surface. Indeed, the Bond albedo of an example pulverized lunar basalt (RELAB ID: LR-CMP-158, originally analyzed in Pieters & Noble 2016) for a Sun-like star is

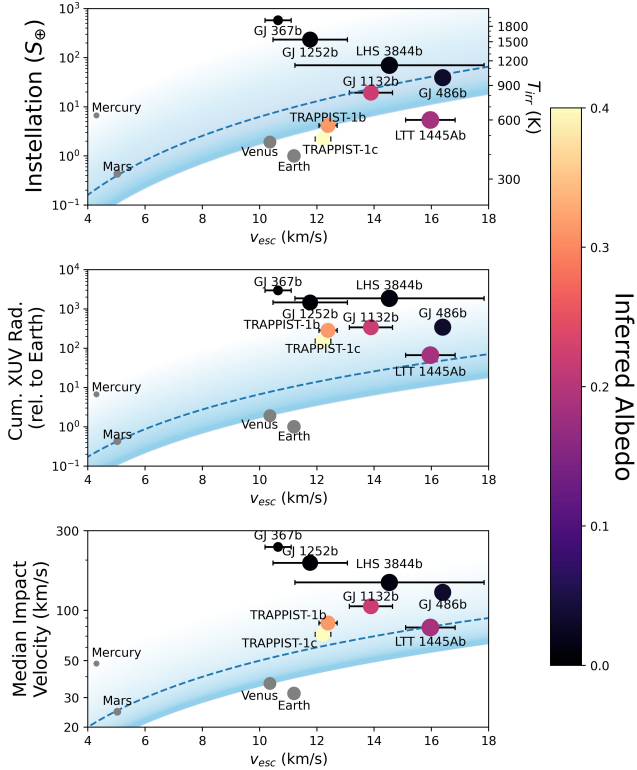


Figure 5. Observed inferred albedo values in the context of the Cosmic Shoreline (Zahnle & Catling 2017) hypothesis, in (top) instellation, (middle) estimated cumulative XUV radiation based on methods outlined in Appendix C, and (bottom) median impact velocity space. Following Zahnle & Catling (2017), median impact velocity is estimated as $v_{imp} \approx \sqrt{v_{esc}^2 + v_{orb}^2}$, where v_{orb} is the Keplerian orbital velocity. The Shorelines follow the scaling laws (top) $v_{esc} \propto I^4$, (middle) $v_{esc} \propto I_{XUV}^4$, and (bottom) $v_{esc} = 5 v_{imp}$. The dotted line is normalized to Mars, whereas the shaded regions are calibrated to Venus and Mercury. The large uncertainty in the exact shoreline position; it is still unclear where the shoreline should lie for M-Earths, and whether it is narrow or wide.

0.23, about twice that of lunar surface soils. Darkening from space weathering is ubiquitous for Solar System airless bodies: $\sim 85\%$ of asteroids exhibit a visual geometric albedo of less than 0.3 despite being petrologically diverse (Wright et al. 2016; Morbidelli et al. 2020). These values are overestimated compared to the true Bond albedo due to the opposition surge effect (Belskaya & Shevchenko 2000). Bond albedos are typically $\sim 40\%$ that of visual geometric albedo given standard assumptions for asteroids (Müller 2007), implying 85% of asteroids have a Bond albedo $\lesssim 0.12$.

It should be noted that the plausibility of fresh, unweathered high-albedo regolith surfaces of M-Earths is not known *a priori*. While M-Earths are subjected to high stellar wind fluxes that promote space weathering,

M-Earths may be subject to higher rates of resurfacing through tidally-induced volcanic activity or frequent impact cratering. Future studies of the geological plausibility of the surface types presented in Hu et al. (2012a) and the expected degree of space weathering on airless M-Earths will be needed to more carefully assess the risk of false positive atmospheric detections through secondary eclipse measurements.

4.3. Future Tests

JWST Cycles 1 – 3 include emission observations of ~ 25 M-Earths. Most of these observations aim to detect or rule out the presence of an atmosphere, either through direct detection of CO_2 spectral features, or indirect detection via atmospheric heat transport. Fig. 7 shows that several of these targets appear favorable when plotted against the instellation-based ‘Cosmic Shoreline’. However, almost all M-Earth targets experienced much more XUV radiation than Earth (due to their low-mass host stars) and likely experienced frequent high-energy impacts (due to their close-in orbits): both are detrimental for atmospheric retention. These results are timely for informing the 500 hour Director’s Discretionary Time (DDT) program to search for atmospheres on M-Earths with MIRI F1500W (Redfield et al. 2024).

Thus, if the DDT survey fails to find conclusive evidence for a substantial M-Earth atmosphere on any target, this would suggest that either cumulative XUV radiation or the energy of impactors, both highly elevated for M-Earths compared to terrestrial planets around FGK stars, are effective at removing atmospheres of small planets. Another possibility is that M-Earths form volatile poor compared to rocky planets in the Solar System (e.g., Desch et al. 2020; Mulders et al. 2015). Such results would motivate atmosphere searches for rocky planets around higher-mass stars. However, emission observations of airless M-Earths would remain useful in probing geological surface processes and crustal compositional diversity of rocky exoplanets, as well as constraining their outgassing and atmospheric loss histories (e.g., Foley 2024; First et al. 2024). As shown in this work, this can be done by assessing and analyzing trends in brightness temperature.

5. CONCLUSIONS

Secondary eclipse data for M-Earths show a tentative trend in the brightness temperature ratio \mathcal{R} as a function of irradiation temperature. The trend is strongly favored statistically over no trend when using the most recent stellar models available for M dwarfs. Options to explain the observed trend include:

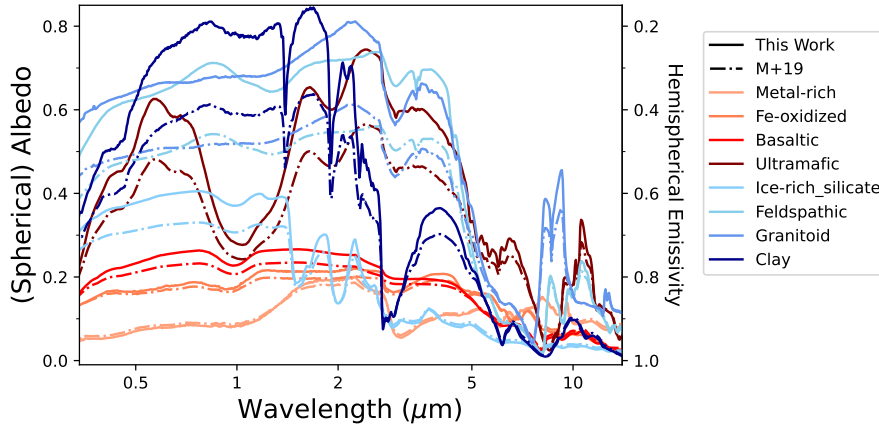


Figure 6. Comparison of spherical albedo values calculated using data from Hu et al. (2012a) used in this study (solid lines) with those in Mansfield et al. (2019) (dash-dotted lines). Colors represent surface types from Hu et al. (2012a).

- Space weathering via micrometeorite impactors and stellar winds darkening faster-orbiting, closer-in planets. However, the degree of space weathering for outer planets would have to be much less than that predicted by the stellar wind strength scaling in Zieba et al. (2023);
- Larger regolith grain sizes caused by higher rates of volcanic resurfacing on close-in, hotter planets or grains sintering at high temperatures;
- Colder, outer planets retain thin outgassed atmospheres while closer-in planets lose (or never gain) such atmospheres quickly due to high atmospheric loss fluxes.

Future observations with JWST will begin to fill in unexplored parameter space (see Fig. 7), which will help to break the degeneracies between each scenario through multi-band or spectroscopic characterization. Combined with the statistical advantages of much larger sample sizes, these observations will provide further constraints on the location of the M-Earth ‘Cosmic Shoreline’.

This work was supported through a NASA grant awarded to the Illinois/NASA Space Grant Consortium. J.I. acknowledges funding from the Alfred P. Sloan Foundation under grant G202114194. M.W.M. and M.Z. acknowledge support from the Heising-Simons Foundation through the 51 Pegasi b Fellowship Program. E.M.-R.K. acknowledges support from the NASA Exoplanets Research Program under grant 80NSSC24K0157.

This research has made use of the NASA Exoplanet Archive, which is operated by the California Institute of Technology, under contract with the National Aeronautics and Space Administration under the Exoplanet Exploration Program. This research utilizes spectra acquired by John F. Mustard and Carle M. Pieters with the NASA RELAB facility at Brown University. The authors thank Mark Hammond for discussions on surface albedo profiles.

APPENDIX

A. DATA FOR TRAPPIST-1 B AND LHS-1478 B

A.1. TRAPPIST-1 b: F1500W vs. F1280W

Early eclipse observations of TRAPPIST-1 b with MIRI 1500W had originally suggested a blackbody-like brightness temperature ($\mathcal{R}_{15\mu\text{m}} \approx 0.99 \pm 0.05$, Greene et al. 2023). This, however, is at odds with more recent eclipse data with F1280W, which suggests a lower brightness temperature at $12.8 \mu\text{m}$ ($\mathcal{R}_{12.8\mu\text{m}} \approx 0.85 \pm 0.06$, Ducrot et al. 2023). Furthermore, reanalysis of the F1500W data suggests a slightly lower eclipse depth, refining the 15 micron brightness temperature to $\mathcal{R}_{15\mu\text{m}} \approx 0.95 \pm 0.05$ (Ducrot et al. 2023). In this work, we use the most up-to-date reduction of both F1280W and F1500W data from Ducrot et al. (2023) (giving a combined $\mathcal{R} \approx 0.91 \pm 0.04$), however we include the original Greene et al. (2023) F1500W eclipse depth results in Fig. 1 and Table 2. TRAPPIST-1 b is the target of

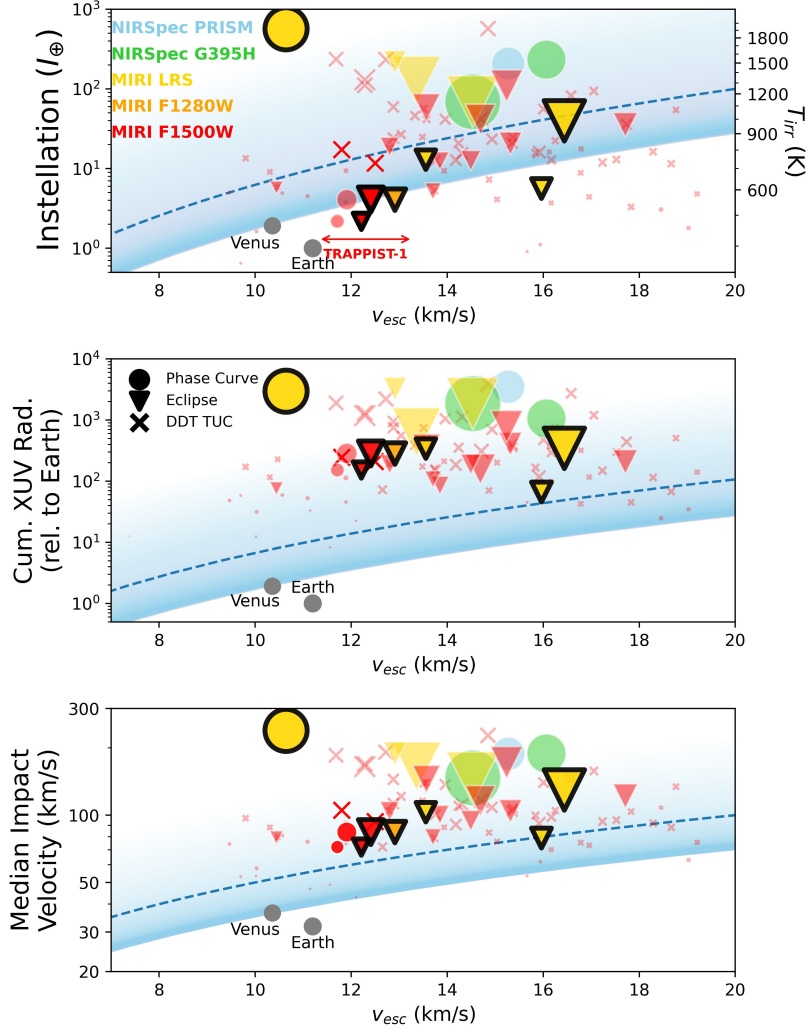


Figure 7. Scheduled M-Earth emission observations for JWST Cycle 1 – 3 and DDT Survey Targets Under Consideration (TUCs) in the context of the Cosmic Shoreline hypothesis: in (top) instellation, (middle) estimated cumulative XUV radiation (see Appendix C), and (bottom) median impactor velocity space. As in Fig. 5, the dotted line is normalized to Mars and the shaded regions are calibrated to Venus and Mercury. Point area represents the estimated relative SNR per instrument+planet setup; SNR is calculated as $ESM \times \sqrt{N_{obs}}$, where $N_{obs} = N_{eclipse} + 4N_{phasecurve}$ (10 eclipses were assumed for TUCs). Planets with black borders represent observations included in this study, all of which lack compelling evidence for thick atmospheres. Separate TRAPPIST-1 observations are offset horizontally for clarity. All data for DDT targets and Cycle 1 – 3 observations not included in this study, except estimated system ages, are from the NASA Exoplanet Archive. Despite many planets seeming like promising candidates for atmospheric retention in terms of their instellation, the high cumulative XUV of their low-mass host stars and high susceptibility to impact-based atmospheric erosion leads to a more pessimistic outlook for the M-Earth opportunity.

future emission observations with JWST using F1500W [GO-3077 (PI: Gillon), GO-5191 (PI: Ducrot)], which will help give more precise constraints on its brightness temperature.

A.2. MIRI F1500W Systematics in Observations of LHS 1478 b

Recent results from the Hot Rocks Survey (Diamond-Lowe et al. 2023) report a shallow MIRI F1500W eclipse depth for the warm ($T_{irr} = 840$ K) M-Earth LHS 1478 b (August et al. 2024). The reported eclipse depth (146 ± 56 ppm) is less than half that expected of a blackbody, and implies an \mathcal{R} value of 0.67 ± 0.10 , significantly lower than any other planet considered in this study. However, these results are complicated by the presence of strong correlated noise in the second visit. Without the use of Gaussian processes to remove this correlated noise, the second eclipse produces a negative eclipse depth that is more than 5σ inconsistent with the first. With the use of Gaussian processes

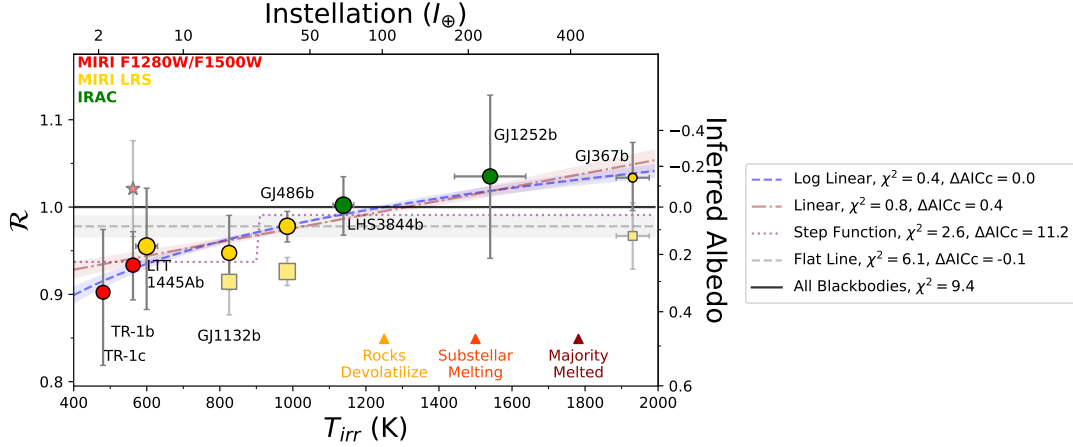


Figure B1. Same as Fig. 1, but with re-derived brightness temperature ratios (\mathcal{R}) using PHOENIX stellar models (Table 2). While a trend is still statistically favored by some metrics (Table 3), ΔAICc suggests the trend and no-trend models and roughly equally likely.

for noise removal, August et al. (2024) still fail to recover the second eclipse. All other planets in this study have shown repeatable or very high confidence ($\gtrsim 5\sigma$) eclipse detections.

B. ADDITIONAL PROCESSES THAT CAN AFFECT BRIGHTNESS TEMPERATURE

B.1. Thermal Beaming from Rough Surfaces

Real planets are not perfect isotropically-scattering spheres nor well-represented by a single blackbody emitter. The thermal emission phase curves of airless rocky bodies in the solar system have a measured disk-integrated emission flux higher than expected from a perfect sphere at low phase angles, and a lower flux at large phase angles (e.g., Lebofsky et al. 1986; Hapke 1996; Emery et al. 1998; Wohlfarth et al. 2023). This effect, known as *thermal beaming*, happens because hotter, more illuminated facets are preferentially tilted towards the host star at opposition, leading to thermal limb brightening. This effect requires macroscopic roughness (typically at the scale of centimeters to millimeters) and negligible heat redistribution (extremely thin or no atmosphere).

We use an advanced thermal roughness model from Wohlfarth et al. (2023) to quantify the effects of thermal beaming on exoplanet eclipse measurements. Following Wohlfarth et al. (2023), we assume a wavelength-albedo profile based on lunar basalt (synthesis of Chandryaan-1 Moon Mineralogy Mapper / M3 data and returned samples). The effects of surface roughness on disk-resolved temperatures for TRAPPIST-1 c is shown in Fig. B2. This is one possible explanation for hot ($T_{\text{irr}} \gtrsim 1500$ K) planets where $\mathcal{R} \gtrsim 1$ —areas near the substellar point are expected to be partially or fully molten and have low albedo (e.g., Essack et al. 2020), while the colder limbs (where brightness temperature differences due to thermal beaming are the largest) remain solid, increasing the disk-integrated brightness temperature higher than that expected of a blackbody.

Using secondary eclipse data alone, the effects of thermal beaming are difficult to distinguish from those of space weathering, as both lead to hotter brightness temperatures. In addition, the dependence of roughness on irradiation temperature is not obvious; sintering at high temperatures near the melting point of rock will likely smoothen surfaces, but closer-in worlds are subject to more frequent micrometeorite impacts that promote roughness. Thermal beaming may be directly detectable with spectroscopic phase curves (Zieba et al. 2023; Tenthoff et al. 2024).

B.2. Tidal Heating

Tidal heating, due to tidal dissipation associated with both orbital circularization and rotational despinning, has been invoked as a possible explanation for dayside temperatures significantly hotter than that expected of a blackbody (e.g., Crossfield et al. 2022; Lyu et al. 2024). However, heating from tidal dissipation becomes negligible once mantle temperatures become hot enough to completely melt rock. This leads to a realistic upper limit of heat transport to the surface on order of $\sim 1 \text{ W m}^{-2}$, which is undetectably small for rocky exoplanets (Henning et al. 2009; Renaud & Henning 2018; Dobos et al. 2019). Although, as discussed earlier, tidal heating may excite volcanic resurfacing, affecting the observed surface composition.

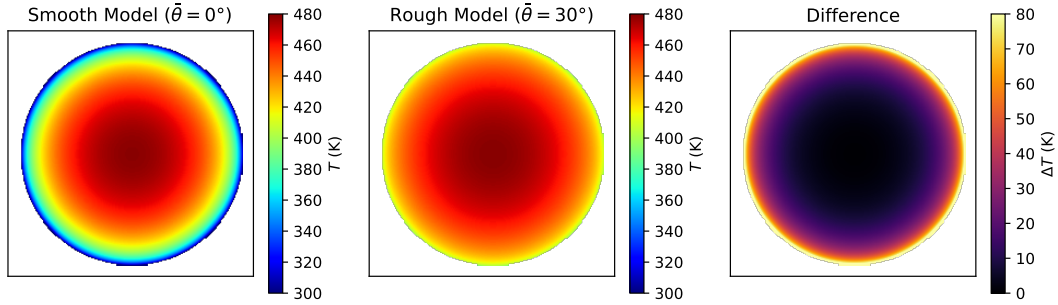


Figure B2. Effects of Moon-like macroscopic surface roughness on disk-resolved brightness temperatures at opposition (i.e., ‘thermal beaming’) for TRAPPIST-1 c, assuming a root-mean-square roughness slope of $\bar{\theta} = 30^\circ$ (see [Wohlfarth et al. 2023](#) for details). Thermal beaming imparts a limb brightening-type effect that increases the disk-integrated brightness temperature (and thus eclipse depth) and may be detectable through phase curve observations ([Zieba et al. 2023](#); [Tenthoff et al. 2024](#)), but is largely indistinguishable from other thermal brightening/surface darkening effects for individual planets with current data.

B.3. *Asynchronous Rotation*

Warm ($T_{irr} > 400$ K) M star rocky planets are assumed to be tidally locked, due to extremely short tidal locking timescales. Asynchronous rotation would result in a dayside cooling dependent on the rotation rate and heat capacity of the surface material (e.g., [Lyu et al. 2024](#)). If close-in planets are tidally locked (1:1 spin:orbit resonance) but further out planets are in a non-1:1 spin-orbit resonance with their host stars, as is the case for Mercury, this could lead to a dichotomy in \mathcal{R} values without invoking the need for an atmosphere. However, tidal locking timescales for planets in this study are extremely short ($\tau_{lock} \lesssim 10^3$ yr) due to their small orbital radii ($\tau_{lock} \propto a^6$). While thick atmospheres may slow down the tidal locking process, modeling suggests that these planets are too close-in for this effect to be significant ([Leconte et al. 2015](#)). Although tidal locking for a rocky exoplanet has only been explicitly shown for LHS 3844 b ([Lyu et al. 2024](#)), follow-up phase curve observations may be able to confirm whether these planets are tidally locked.

B.4. *Aerosols*

The atmospheres tested in the thin atmosphere hypothesis of §3.3 were assumed to be clear (absent of aerosols or clouds). However, aerosols and clouds are ubiquitous in the atmospheres of rocky planets in the Solar System (including Titan) and have been observed to be also prevalent in (albeit non-“rocky”) exoplanets that span similar equilibrium temperatures to those analyzed here ([Kempton et al. 2023](#); [Beatty et al. 2024](#)). The presence of aerosols and clouds can have two separate effects. Firstly, hazes in the planet’s dayside atmosphere can efficiently absorb incident stellar light at shorter wavelengths and thereby create a thermal inversion—i.e., a stratosphere that is hotter than at pressures deeper below (e.g., [Hu et al. 2012b](#)). This “flips” atmospheric features to be observed in emission rather than absorption. For narrow band observations covering specific absorption features, the inverted emission feature could potentially cancel out the effects of redistributive cooling and lead to a low inferred albedo. For rocky planets around M stars in particular, even the near infrared molecular absorption of H_2O can serve this role (?), but hazes can potentially be even more efficient absorbers and have a greater impact on the thermal profile.

To test whether this effect can produce a false negative for a thick atmosphere, we forward model 10 bar CO_2 atmospheres that have Titan-like tholin hazes, using the optical properties from [Kitzmann & Heng \(2018\)](#). Given that such hazes form via UV photochemistry on Titan, it is possible that they also readily form around these planets, which are closer in and orbit M stars that radiate high amounts of UV ([Peacock et al. 2019](#)). In lieu of detailed photochemical and microphysics modeling, we focus on end member scenarios and assume vertically fixed volume mixing ratios (VMRs) of 10^{-16} - 10^{-10} in 1-dex intervals (the effect may be non-monotonic). This roughly spans the range of haze VMR observed in Titan’s atmosphere ([Fan et al. 2019](#)). We use two log-normal particle size distributions of varying means to match lab experiment results in ([He et al. 2020](#)). We show the range of derived \mathcal{R} in Figure B3. While we indeed find thermal inversions in the temperature-pressure profiles of some of these atmospheres, we find it unlikely that any of the current observations could serve as a false negative due to a haze-induced thermal inversion.

Secondly, another effect that can potentially affect the dayside heat budget and give rise to a false negative is the preferential formation of clouds on the nightside of the planet. Such clouds, if optically thick, can inhibit radiative

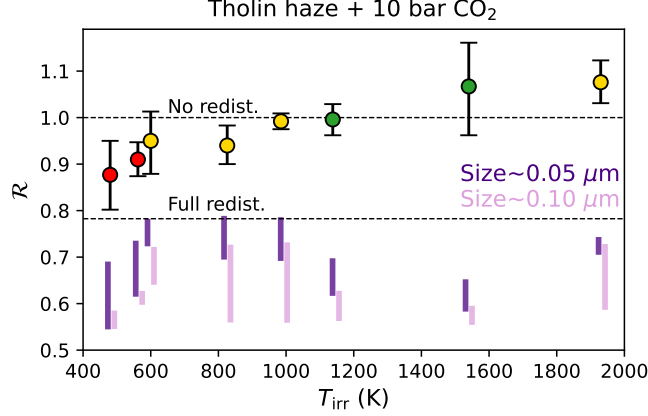


Figure B3. Modeled brightness temperature ratios of thick, hazy atmospheres, for two particle size distributions of Titan-like tholin hazes. The range in brightness temperature ratios for each planet spans the modeled volume mixing ratios of haze particles ($10^{-16} - 10^{-10}$), assumed to be vertically constant. The rest of the atmosphere is comprised of 10 bars of CO_2 . Brightness temperatures are calculated in the bandpass of each instrument. While Titan-like hazes can have a large effect on \mathcal{R} , we do not find a false negative scenario for a thick atmosphere.

cooling and trap the heat via efficient greenhouse effect on the night side, resulting in a net warming (e.g., Turbet et al. 2021). Additionally, the clouds give rise to the nightside emission emerging from lower pressures than the dayside emission; this could in turn exaggerate the day/night brightness temperature contrast relative to the actual temperatures at the surface (Powell et al. 2024). This effect has only been highlighted for rocky planets around M stars recently in Powell et al. (2024) and require a somewhat narrow range of temperatures for preferential formation of nightside clouds. Global circulation models across a broader parameter space in the future will be necessary to establish in what regimes nightside clouds can be false negatives for thick atmospheres.

C. XUV MODEL

To estimate the cumulative XUV irradiation experienced by the planets in this work, we follow the simplified broken power law approach of Rogers et al. (2021). In this framework,

$$\frac{L_{XUV}}{L_{bol}} = \begin{cases} 10^{-3.5} \left(\frac{M_*}{M_\odot}\right)^{-0.5} & \text{for } t < t_{sat}, \\ 10^{-3.5} \left(\frac{M_*}{M_\odot}\right)^{-0.5} \left(\frac{t}{t_{sat}}\right)^{-1.5} & \text{for } t \geq t_{sat}. \end{cases} \quad (\text{C1})$$

where L_{bol} is the bolometric luminosity, L_{XUV} is the XUV luminosity, M_* is the star mass, and t_{sat} is the ‘saturation time’ defined by

$$t_{sat} = 10^2 \left(\frac{M_*}{M_\odot}\right)^{-1.0} \text{ Myr}. \quad (\text{C2})$$

We use empirical isochrones derived for low-mass stars from Herczeg & Hillenbrand (2015) to estimate host stars’ bolometric luminosity as a function of mass and time. We highlight that, as noted in Zahnle & Catling (2017), the pre-saturation phase is the dominant contributor to the total XUV radiation. The model is then run through for the entire estimated system age, ignoring error estimates for simplicity (see Table C1). Lower limits were used in cases of poorly-constrained ages. For systems without estimated ages, we use the simple scaling law presented in Zahnle & Catling (2017):

$$I_{XUV} = \frac{I}{I_\oplus} \left(\frac{L_*}{L_\odot}\right)^{-0.6}, \quad (\text{C3})$$

where I_{XUV} is the estimated cumulative XUV flux relative to Earth, I is the planet’s present-day instellation (relative to Earth), and L_* is the luminosity of the host star (relative to the Sun). This approach was consistent within a factor of ~ 2.5 with our time-evolution model for all planets.

Table C1. System Age Values Used in this Study

System	Age (Gyr)	Reference
TRAPPIST-1	7.6	Burgasser & Mamajek (2017)
GJ 1132	6.31	Gaidos et al. (2023)
GJ 486	3.51	Gaidos et al. (2023)
LHS 3844	7.8	Kane et al. (2020)
GJ 1252	6.61	Gaidos et al. (2023)
GJ 367	7.95	Gaidos et al. (2023)
LTT 1445 A	2	Rukdee et al. (2024)
GJ 357	> 5	Modirrousta-Galian et al. (2020)
GJ 806	4	Palle et al. (2023)
HD 260655	3	Luque et al. (2022)
LHS 1140	> 5	Dittmann et al. (2017)
LP 791-18	> 0.5	Crossfield et al. (2019)
LTT 3780	3.1	Bonfanti et al. (2024)
TOI-1468	> 1	Chaturvedi et al. (2022)
TOI-1685	1.3	Burt et al. (2024)
TOI-1075	> 2	Essack et al. (2023)

There is large uncertainty in the time evolution of both bolometric and XUV fluxes, especially for the low mass M stars in this work (e.g., France et al. 2022; Diamond-Lowe et al. 2024). The values shown in Figures 5 and 7 should be seen as rough estimations.

REFERENCES

- Agol, E., Dorn, C., Grimm, S. L., et al. 2021, PSJ, 2, 1, doi: [10.3847/PSJ/abd022](https://doi.org/10.3847/PSJ/abd022)
- Anderson, D. R., & Burnham, K. P. 2002, The Journal of wildlife management, 912
- August, P. C., Buchhave, L. A., Diamond-Lowe, H., et al. 2024, Hot Rocks Survey I : A shallow eclipse for LHS 1478 b. <https://arxiv.org/abs/2410.11048>
- Barstow, J. K., & Irwin, P. G. J. 2016, MNRAS, 461, L92, doi: [10.1093/mnrasl/slw109](https://doi.org/10.1093/mnrasl/slw109)
- Beatty, T. G., Welbanks, L., Schlawin, E., et al. 2024, ApJL, 970, L10, doi: [10.3847/2041-8213/ad55e9](https://doi.org/10.3847/2041-8213/ad55e9)
- Belskaya, I., & Shevchenko, V. 2000, Icarus, 147, 94
- Bergin, E. A., Kempton, E. M.-R., Hirschmann, M., et al. 2023, The Astrophysical Journal Letters, 949, L17
- Bonfanti, A., Brady, M., Wilson, T., et al. 2024, Astronomy & Astrophysics, 682, A66
- Burgasser, A. J., & Mamajek, E. E. 2017, The Astrophysical Journal, 845, 110
- Burt, J. A., Hooton, M. J., Mamajek, E. E., et al. 2024, arXiv preprint arXiv:2405.14895
- Chapman, C. R. 2004, Annu. Rev. Earth Planet. Sci., 32, 539
- Chaturvedi, P., Bluhm, P., Nagel, E., et al. 2022, Astronomy & Astrophysics, 666, A155
- Cowan, N. B., & Agol, E. 2011, The Astrophysical Journal, 729, 54
- Crossfield, I. J., Waalkes, W., Newton, E. R., et al. 2019, The Astrophysical Journal, 883, L16
- Crossfield, I. J. M., Malik, M., Hill, M. L., et al. 2022, ApJL, 937, L17, doi: [10.3847/2041-8213/ac886b](https://doi.org/10.3847/2041-8213/ac886b)
- Davenport, J. R., Becker, A. C., Kowalski, A. F., et al. 2012, The Astrophysical Journal, 748, 58
- Deming, D., Seager, S., Winn, J., et al. 2009, PASP, 121, 952, doi: [10.1086/605913](https://doi.org/10.1086/605913)
- Desch, S. J., Abbot, D., Krijt, S., et al. 2020, in Planetary Diversity: Rocky planet processes and their observational signatures (IOP Publishing Bristol, UK), 6–1
- Diamond-Lowe, H., Youngblood, A., Charbonneau, D., et al. 2021, The Astronomical Journal, 162, 10

- Diamond-Lowe, H., Mendonca, J. M., Akin, C. J., et al. 2023, The Hot Rocks Survey: Testing 9 Irradiated Terrestrial Exoplanets for Atmospheres, JWST Proposal. Cycle 2, ID. #3730
- Diamond-Lowe, H., King, G., Youngblood, A., et al. 2024, *Astronomy & Astrophysics*, 689, A48
- Dittmann, J. A., Irwin, J. M., Charbonneau, D., et al. 2017, *Nature*, 544, 333
- Dobos, V., Barr, A. C., & Kiss, L. L. 2019, *Astronomy & Astrophysics*, 624, A2
- Dong, C., Jin, M., Lingam, M., et al. 2018, *Proceedings of the National Academy of Sciences*, 115, 260
- Ducrot, E., Lagage, P.-O., Min, M., et al. 2023, doi: [10.21203/rs.3.rs-3706919/v1](https://doi.org/10.21203/rs.3.rs-3706919/v1)
- Emery, J., Sprague, A., Witteborn, F., et al. 1998, *Icarus*, 136, 104
- Essack, Z., Seager, S., & Pajusalu, M. 2020, *The Astrophysical Journal*, 898, 160
- Essack, Z., Shporer, A., Burt, J. A., et al. 2023, *The Astronomical Journal*, 165, 47
- Fan, S., Shemansky, D. E., Li, C., et al. 2019, *Earth and Space Science*, 6, 1057, doi: <https://doi.org/10.1029/2018EA000477>
- Fazio, G., Hora, J., Allen, L., et al. 2004, *The Astrophysical Journal Supplement Series*, 154, 10
- Fernandes, R. B., Mulders, G. D., Pascucci, I., Mordasini, C., & Emsenhuber, A. 2019, *The Astrophysical Journal*, 874, 81
- First, E. C., Mishra, I., Gazel, E., et al. 2024, *Nature Astronomy*, 1
- Fischer, E. M., & Pieters, C. M. 1994, *Icarus*, 111, 475
- Foley, B. J. 2024, *Reviews in Mineralogy and Geochemistry*, 90, 559
- France, K., Fleming, B., Youngblood, A., et al. 2022, *Journal of Astronomical Telescopes, Instruments, and Systems*, 8, 014006, doi: [10.1117/1.JATIS.8.1.014006](https://doi.org/10.1117/1.JATIS.8.1.014006)
- Gaidos, E., Claytor, Z., Dungee, R., Ali, A., & Feiden, G. A. 2023, *Monthly Notices of the Royal Astronomical Society*, 520, 5283
- Goffo, E., Gandolfi, D., Egger, J. A., et al. 2023, *The Astrophysical Journal Letters*, 955, L3
- Greene, T. P., Bell, T. J., Ducrot, E., et al. 2023, *Nature*, 618, 39
- Hammond, M., Guimond, C. M., Lichtenberg, T., et al. 2024, arXiv preprint arXiv:2409.04386
- Hansen, B. M. 2008, *The Astrophysical Journal Supplement Series*, 179, 484
- Hapke, B. 1977, *Physics of the Earth and Planetary Interiors*, 15, 264
- . 1996, *Journal of Geophysical Research: Planets*, 101, 16833
- . 2001, *Journal of Geophysical Research: Planets*, 106, 10039
- . 2012, *Theory of reflectance and emittance spectroscopy* (Cambridge University Press)
- He, C., Hörst, S. M., Lewis, N. K., et al. 2020, *Nature Astronomy*, 4, 986, doi: [10.1038/s41550-020-1072-9](https://doi.org/10.1038/s41550-020-1072-9)
- Henning, W. G., O'Connell, R. J., & Sasselov, D. D. 2009, *The Astrophysical Journal*, 707, 1000
- Herczeg, G. J., & Hillenbrand, L. A. 2015, *The Astrophysical Journal*, 808, 23
- Hirschmann, M. M., Bergin, E. A., Blake, G. A., Ciesla, F. J., & Li, J. 2021, *Proceedings of the National Academy of Sciences*, 118, e2026779118
- Hu, R., Ehlmann, B. L., & Seager, S. 2012a, *ApJ*, 752, 7, doi: [10.1088/0004-637X/752/1/7](https://doi.org/10.1088/0004-637X/752/1/7)
- Hu, R., Seager, S., & Bains, W. 2012b, *ApJ*, 761, 166, doi: [10.1088/0004-637X/761/2/166](https://doi.org/10.1088/0004-637X/761/2/166)
- Husser, T.-O., Wende-von Berg, S., Dreizler, S., et al. 2013, *Astronomy & Astrophysics*, 553, A6
- Ih, J., Kempton, E. M.-R., Whittaker, E. A., & Lessard, M. 2023, *The Astrophysical Journal Letters*, 952, L4
- Iyer, A. R., Line, M. R., Muirhead, P. S., Fortney, J. J., & Gharib-Nezhad, E. 2023, *The Astrophysical Journal*, 944, 41
- Jackson, B., Barnes, R., & Greenberg, R. 2008, *Monthly Notices of the Royal Astronomical Society*, 391, 237
- Jost, B., Pommerol, A., Poch, O., et al. 2016, *Icarus*, 264, 109
- Kane, S. R., Roettenbacher, R. M., Unterborn, C. T., Foley, B. J., & Hill, M. L. 2020, *The Planetary Science Journal*, 1, 36
- Kempton, E. M. R., Zhang, M., Bean, J. L., et al. 2023, *Nature*, 620, 67, doi: [10.1038/s41586-023-06159-5](https://doi.org/10.1038/s41586-023-06159-5)
- Keppler, H., & Golabek, G. 2019, *Geochemical Perspectives Letters*, 11, 12
- King, G. W., & Wheatley, P. J. 2021, *Monthly Notices of the Royal Astronomical Society: Letters*, 501, L28
- Kite, E. S., & Barnett, M. N. 2020, *Proceedings of the National Academy of Sciences*, 117, 18264
- Kite, E. S., & Schaefer, L. 2021, *The Astrophysical Journal Letters*, 909, L22
- Kitzmann, D., & Heng, K. 2018, *MNRAS*, 475, 94, doi: [10.1093/mnras/stx3141](https://doi.org/10.1093/mnras/stx3141)
- Koll, D. D. B. 2022, *ApJ*, 924, 134, doi: [10.3847/1538-4357/ac3b48](https://doi.org/10.3847/1538-4357/ac3b48)
- Koll, D. D. B., Malik, M., Mansfield, M., et al. 2019, *ApJ*, 886, 140, doi: [10.3847/1538-4357/ab4c91](https://doi.org/10.3847/1538-4357/ab4c91)

- Kral, Q., Wyatt, M. C., Triaud, A. H., et al. 2018, *Monthly Notices of the Royal Astronomical Society*, 479, 2649
- Kreidberg, L., Koll, D. D. B., Morley, C., et al. 2019, *Nature*, 573, 87, doi: [10.1038/s41586-019-1497-4](https://doi.org/10.1038/s41586-019-1497-4)
- Krijt, S., Kama, M., McClure, M., et al. 2022, arXiv preprint arXiv:2203.10056
- Krissansen-Totton, J. 2023, *The Astrophysical Journal Letters*, 951, L39
- Lebofsky, L. A., Sykes, M. V., Tedesco, E. F., et al. 1986, *Icarus*, 68, 239
- Leconte, J., Wu, H., Menou, K., & Murray, N. 2015, *Science*, 347, 632, doi: [10.1126/science.1258686](https://doi.org/10.1126/science.1258686)
- Li, J., Bergin, E. A., Blake, G. A., Ciesla, F. J., & Hirschmann, M. M. 2021, *Science Advances*, 7, eabd3632
- Lincowski, A. P., Meadows, V. S., Zieba, S., et al. 2023, *The Astrophysical Journal Letters*, 955, L7
- Lucey, P. G., Taylor, G. J., & Malaret, E. 1995, *Science*, 268, 1150
- Luo, H., O'Rourke, J. G., & Deng, J. 2024, *Science Advances*, 10, eado7603
- Luque, R., Fulton, B., Kunimoto, M., et al. 2022, *Astronomy & Astrophysics*, 664, A199
- Lustig-Yaeger, J., Meadows, V. S., & Lincowski, A. P. 2019, *The Astronomical Journal*, 158, 27
- Lutgens, F. K., Tarbuck, E. J., & Tasa, D. 2000, *Essentials of geology*, Vol. 480 (Prentice Hall Upper Saddle River, NJ)
- Lyu, X., Koll, D. D., Cowan, N. B., et al. 2024, *The Astrophysical Journal*, 964, 152
- Malik, M., Kempton, E. M. R., Koll, D. D. B., et al. 2019, *ApJ*, 886, 142, doi: [10.3847/1538-4357/ab4a05](https://doi.org/10.3847/1538-4357/ab4a05)
- Malik, M., Grosheintz, L., Mendonça, J. M., et al. 2017, *AJ*, 153, 56, doi: [10.3847/1538-3881/153/2/56](https://doi.org/10.3847/1538-3881/153/2/56)
- Mallama, A., Wang, D., & Howard, R. A. 2002, *Icarus*, 155, 253
- Mansfield, M., Kite, E. S., Hu, R., et al. 2019, *ApJ*, 886, 141, doi: [10.3847/1538-4357/ab4c90](https://doi.org/10.3847/1538-4357/ab4c90)
- Marcq, E., Mills, F. P., Parkinson, C. D., & Vandaele, A. C. 2018, *SSRv*, 214, 10, doi: [10.1007/s11214-017-0438-5](https://doi.org/10.1007/s11214-017-0438-5)
- Matthews, G. 2008, *Applied optics*, 47, 4981
- Mergny, C., & Schmidt, F. 2024, *The Planetary Science Journal*, 5, 216
- Modirrousta-Galian, D., Stelzer, B., Magaudda, E., et al. 2020, *Astronomy & Astrophysics*, 641, A113
- Montet, B. T., Crepp, J. R., Johnson, J. A., Howard, A. W., & Marcy, G. W. 2014, *The Astrophysical Journal*, 781, 28
- Morbidelli, A., Delbo, M., Granvik, M., et al. 2020, *Icarus*, 340, 113631
- Mulders, G. D., Ciesla, F. J., Min, M., & Pascucci, I. 2015, *The Astrophysical Journal*, 807, 9
- Müller, M. 2007, Phd thesis, Freie Universität Berlin
- Nakayama, A., Ikoma, M., & Terada, N. 2022, *The Astrophysical Journal*, 937, 72
- Noble, S. K., Pieters, C. M., & Keller, L. P. 2007, *Icarus*, 192, 629
- Olson, S. L., Schwietzman, E. W., Reinhard, C. T., & Lyons, T. W. 2018, in *Handbook of Exoplanets*, ed. H. J. Deeg & J. A. Belmonte, 189, doi: [10.1007/978-3-319-55333-7_189](https://doi.org/10.1007/978-3-319-55333-7_189)
- Palle, E., Orell-Miquel, J., Brady, M., et al. 2023, *Astronomy & Astrophysics*, 678, A80
- Peacock, S., Barman, T., Shkolnik, E. L., Hauschildt, P. H., & Baron, E. 2019, *ApJ*, 871, 235, doi: [10.3847/1538-4357/aaf891](https://doi.org/10.3847/1538-4357/aaf891)
- Peng, B., & Valencia, D. 2024, arXiv e-prints, arXiv:2405.08998, doi: [10.48550/arXiv.2405.08998](https://doi.org/10.48550/arXiv.2405.08998)
- Pieters, C. M., & Noble, S. K. 2016, *Journal of Geophysical Research: Planets*, 121, 1865
- Pontoppidan, K. M., Pickering, T. E., Laidler, V. G., et al. 2016, in *Observatory operations: Strategies, processes, and systems vi*, Vol. 9910, SPIE, 381–395
- Powell, D., Wordsworth, R., & Öberg, K. 2024, arXiv preprint arXiv:2409.07542
- Raftery, A. E. 1995, *Sociological methodology*, 111
- Redfield, S., Batalha, N., Benneke, B., et al. 2024, arXiv e-prints, arXiv:2404.02932, doi: [10.48550/arXiv.2404.02932](https://doi.org/10.48550/arXiv.2404.02932)
- Renaud, J. P., & Henning, W. G. 2018, *The Astrophysical Journal*, 857, 98
- Ribas, I., Bolmont, E., Selsis, F., et al. 2016, *Astronomy & Astrophysics*, 596, A111
- Rieke, G. H., Wright, G., Böker, T., et al. 2015, *Publications of the Astronomical Society of the Pacific*, 127, 584
- Rogers, J. G., Gupta, A., Owen, J. E., & Schlichting, H. E. 2021, *Monthly Notices of the Royal Astronomical Society*, 508, 5886
- Rukdee, S., Buchner, J., Burwitz, V., et al. 2024, *A&A*, 687, A237, doi: [10.1051/0004-6361/202449400](https://doi.org/10.1051/0004-6361/202449400)
- Schlichting, H. E., & Mukhopadhyay, S. 2018, *Space Science Reviews*, 214, 1
- Seager, S. 2013, *Science*, 340, 577
- Segura, A., Walkowicz, L. M., Meadows, V., Kasting, J., & Hawley, S. 2010, *Astrobiology*, 10, 751
- Shields, A. L., Ballard, S., & Johnson, J. A. 2016, *Physics Reports*, 663, 1
- Shporer, A., Collins, K. A., Astudillo-Defru, N., et al. 2020, *ApJL*, 890, L7, doi: [10.3847/2041-8213/ab7020](https://doi.org/10.3847/2041-8213/ab7020)

- Speagle, J. S. 2020, *Monthly Notices of the Royal Astronomical Society*, 493, 3132
- STScI Development Team. 2013, *pysynphot*: Synthetic photometry software package, *Astrophysics Source Code Library*, record ascl:1303.023
- Taylor, G. J., Boynton, W., Brückner, J., et al. 2006, *Journal of Geophysical Research: Planets*, 111
- Taylor, S. R., & McLennan, S. M. 2001, *Encyclopedia of physical science and technology*, 312, 697
- Tenthoff, M., Wohlfarth, K., Wöhler, C., Zieba, S., & Kreidberg, L. 2024, *Reflectance and Emission Modelling of Airless Exoplanets*, Tech. rep., Copernicus Meetings
- Turbet, M., Bolmont, E., Chaverot, G., et al. 2021, *Nature*, 598, 276, doi: [10.1038/s41586-021-03873-w](https://doi.org/10.1038/s41586-021-03873-w)
- Vanderspek, R., Huang, C. X., Vanderburg, A., et al. 2019, *ApJL*, 871, L24, doi: [10.3847/2041-8213/aaf7a](https://doi.org/10.3847/2041-8213/aaf7a)
- Wachiraphan, P., Berta-Thompson, Z. K., Diamond-Lowe, H., et al. 2024, arXiv preprint arXiv:2410.10987
- Weiner Mansfield, M., Xue, Q., Zhang, M., et al. 2024, *The Astrophysical Journal Letters*, 975, L22
- Whittaker, E. A., Malik, M., Ih, J., et al. 2022, *AJ*, 164, 258, doi: [10.3847/1538-3881/ac9ab3](https://doi.org/10.3847/1538-3881/ac9ab3)
- Winter, J. D. 2014, *Principles of igneous and metamorphic petrology*, Vol. 2 (Pearson education Harlow, UK)
- Wohlfarth, K., Wöhler, C., Hiesinger, H., & Helbert, J. 2023, *Astronomy & Astrophysics*, 674, A69
- Wright, E. L., Mainzer, A., Masiero, J., Grav, T., & Bauer, J. 2016, *The Astronomical Journal*, 152, 79
- Wyatt, M., Kral, Q., & Sinclair, C. 2020, *Monthly Notices of the Royal Astronomical Society*, 491, 782
- Xue, Q., Bean, J. L., Zhang, M., et al. 2024, *The Astrophysical Journal Letters*, 973, L8
- Zahnle, K. J., & Catling, D. C. 2017, *ApJ*, 843, 122, doi: [10.3847/1538-4357/aa7846](https://doi.org/10.3847/1538-4357/aa7846)
- Zaini, N., Van der Meer, F., & Van der Werff, H. 2012, *Remote sensing*, 4, 987
- Zhang, M., Hu, R., Inglis, J., et al. 2024, *The Astrophysical Journal Letters*, 961, L44
- Zhuang, Y., Zhang, H., Ma, P., et al. 2023, *Icarus*, 391, 115346
- Zieba, S., Hu, R., Kreidberg, L., et al. 2023, *The search for regolith on the airless exoplanet LHS 3844 b, JWST Proposal. Cycle 2, ID. #4008*
- Zieba, S., Kreidberg, L., Ducrot, E., et al. 2023, *Nature*, 1